

Supporting Information

I.	Experimental Details	S1
II.	ATR-IR Spectroscopic Investigation	S4
III.	X-Ray Powder Diffraction and Le Bail Fit	S5
IV.	Crystal Structure Solution and Refinement Details	S12
V.	Magnetic Properties	S20
VI.	Computational Methods	S34
VII.	References	S39

I. Experimental Details

Materials and Methods

All manipulations were carried out using break-and-seal and glove-box techniques¹ under an atmosphere of argon. Tetrahydrofuran (THF) and hexanes were (Sigma-Aldrich) were dried over Na/benzophenone and distilled prior to use. THF-*d*₈ (Sigma Aldrich) was dried over NaK₂ alloy and vacuum-transferred. Cyclooctatetraene (COT, 98%), potassium (98%), CaI₂ (99.95%), and TmCl₃ (99%) were purchased from Sigma Aldrich and used as received. GdCl₃ (99.9%), TbCl₃ (99.9%), DyCl₃ (99.9%), HoCl₃ (99.9%), ErCl₃ (99.9%), and YbCl₃ (99.9%) were purchased from Strem Chemicals and used as received. K₂COT was prepared as described previously.² Attenuated total reflection (ATR) spectra were recorded on a Perkin-Elmer Spectrum 100 FT-IR spectrometer. Photoluminescence (PL) measurements were performed on a Horiba Fluoromax 4 spectrometer. The X-ray powder diffraction data were collected on a Bruker D8 Advance diffractometer (Cu K α radiation, focusing Göbel Mirror, LynxEye one-dimensional detector, a step of 0.02° 2 θ , 20 °C). The crystalline samples under investigation were ground under Ar in the glove-box and placed in the dome-like airtight zero background holders. Le Bail fit for powder diffraction patterns was performed using TOPAS, version 4 software package (Bruker AXS, 2006).

[GdKCa(COT)₃(THF)₃] (1-Gd)

CaI₂ (16 mg, 0.055 mmol) and GdCl₃ (15 mg, 0.055 mmol) were stirred in THF (5.0 mL) under an argon atmosphere at 25 °C for 24 hours. Slow addition of K₂COT (30 mg, 0.17 mmol, in 2.0 mL of THF) to a violently stirred solution produced a cloudy yellow mixture with a large amount of white precipitate formed in 30 minutes. The mixture was allowed to stir under an argon atmosphere at 25 °C for 48 hours to complete the reaction. The suspension was then filtered, and the yellow filtrate was layered with 2.5 mL of anhydrous hexanes. The ampule was sealed under argon and stored at 5 °C. Orange-yellow blocks were present in good yield after 5 days. Yield: 34 mg, 80%. ATR-IR: 677, 876, 888, 1030 cm⁻¹.

[TbKCa(COT)₃(THF)₃] (2-Tb)

CaI₂ (16 mg, 0.055 mmol) and TbCl₃ (15 mg, 0.055 mmol) were stirred in THF (5.0 mL) under an argon atmosphere at 25 °C for 24 hours. Slow addition of K₂COT (30 mg, 0.17 mmol, in 2.0 mL of THF) to a violently stirred solution produced a cloudy yellow mixture with a large amount of white precipitate formed in 30 minutes. The mixture was allowed to stir under an argon atmosphere at 25 °C for 48 hours to complete the reaction. The suspension was filtered, and the yellow-orange filtrate was layered with 2.5

mL of anhydrous hexanes. The ampule was sealed under argon and stored at 5 °C. Yellow blocks were present in good yield after 4 days. Yield: 30 mg, 70%. ATR-IR: 677, 876, 888, 1030 cm⁻¹.

[DyKCa(COT)₃(THF)₃] (3-Dy)

CaI₂ (16 mg, 0.055 mmol) and DyCl₃ (15 mg, 0.055 mmol) were stirred in THF (5.0 mL) under an argon atmosphere at 25 °C for 24 hours. Slow addition of K₂COT (30 mg, 0.17 mmol, in 2.0 mL of THF) to a violently stirred solution produced a cloudy yellow solution with a large amount of white precipitate formed in 30 minutes. The mixture was allowed to stir under an argon atmosphere at 25 °C for 48 hours to complete the reaction. The suspension was filtered, and the yellow filtrate was layered with 2.5 mL of anhydrous hexanes. The ampule was sealed under argon and stored at 5 °C. Yellow blocks were present in good yield after 3 days. Yield: 34 mg, 80%. ATR-IR: 677, 876, 888, 1030 cm⁻¹.

[HoKCa(COT)₃(THF)₃] (4-Ho)

CaI₂ (16 mg, 0.055 mmol) and HoCl₃ (15 mg, 0.055 mmol) were stirred in THF (5.0 mL) under an argon atmosphere at 25 °C for 24 hours. Slow addition of K₂COT (30 mg, 0.17 mmol, in 2.0 mL of THF) to a violently stirred solution produced a cloudy yellow solution with a large amount of white precipitate formed in 30 minutes. The mixture was allowed to stir under an argon atmosphere at 25 °C for 48 hours to complete the reaction. The suspension was filtered, and the yellow filtrate was layered with 2.5 mL of anhydrous hexanes. The ampule was sealed under argon and stored at 5 °C. Yellow blocks were present in good yield after 5 days. Yield: 35 mg, 86%. ATR-IR: 678, 875, 888, 1030 cm⁻¹.

[ErKCa(COT)₃(THF)₃] (5-Er)

CaI₂ (16 mg, 0.055 mmol) and ErCl₃ (15 mg, 0.055 mmol) were stirred in THF (5.0 mL) under an argon atmosphere at 25 °C for 24 hours. Slow addition of K₂COT (30 mg, 0.17 mmol, in 2.0 mL of THF) to a violently stirred solution produced a cloudy yellow solution with a large amount of white precipitate formed in 30 minutes. The mixture was allowed to stir under an argon atmosphere at 25 °C for 48 hours to complete the reaction. The suspension was filtered, and the pink-orange filtrate was layered with 2.5 mL of anhydrous hexanes. The ampule was sealed under argon and stored at 5 °C. Yellow blocks were present in good yield after 5 days. Yield: 35 mg, 82%. ATR-IR: 679, 875, 889, 1030 cm⁻¹.

[TmKCa(COT)₃(THF)₃] (6-Tm)

CaI₂ (16 mg, 0.055 mmol) and TmCl₃ (15 mg, 0.055 mmol) were stirred in THF (5.0 mL) under an argon atmosphere at 25 °C for 24 hours. Slow addition of K₂COT (30 mg, 0.17 mmol, in 2.0 mL of THF) to a violently stirred solution produced a cloudy orange solution with a large amount of white precipitate formed in 30 minutes. The mixture was allowed to stir under an argon atmosphere at 25 °C for 48 hours to complete the reaction. The suspension was filtered, and the orange filtrate was layered with 2.5 mL of anhydrous hexanes. The ampule was sealed under argon and stored at 5 °C. Orange blocks were present in good yield after 6 days. Yield: 32 mg, 75%. ATR-IR: 679, 875, 889, 1030 cm⁻¹.

[YbKCa(COT)₃(THF)₃] (7-Yb)

CaI₂ (16 mg, 0.055 mmol) and YbCl₃ (15 mg, 0.055 mmol) were stirred in THF (5.0 mL) under an argon atmosphere at 25 °C for 24 hours. Slow addition of K₂COT (30 mg, 0.17 mmol, in 2.0 mL of THF) to a violently stirred solution produced a cloudy blue solution with a large amount of white precipitate in formed in 30 minutes. The mixture was allowed to stir under an argon atmosphere at 25 °C for 48 hours to complete the reaction. The suspension was filtered, and the blue filtrate was layered with 2.5 mL of anhydrous hexanes. The ampule was sealed under argon and stored at 5 °C. Blue blocks were present in good yield after 5 days. Yield: 35 mg, 81%. ATR-IR: 679, 875, 889, 1030 cm⁻¹.

II. ATR-IR Spectroscopic Investigation

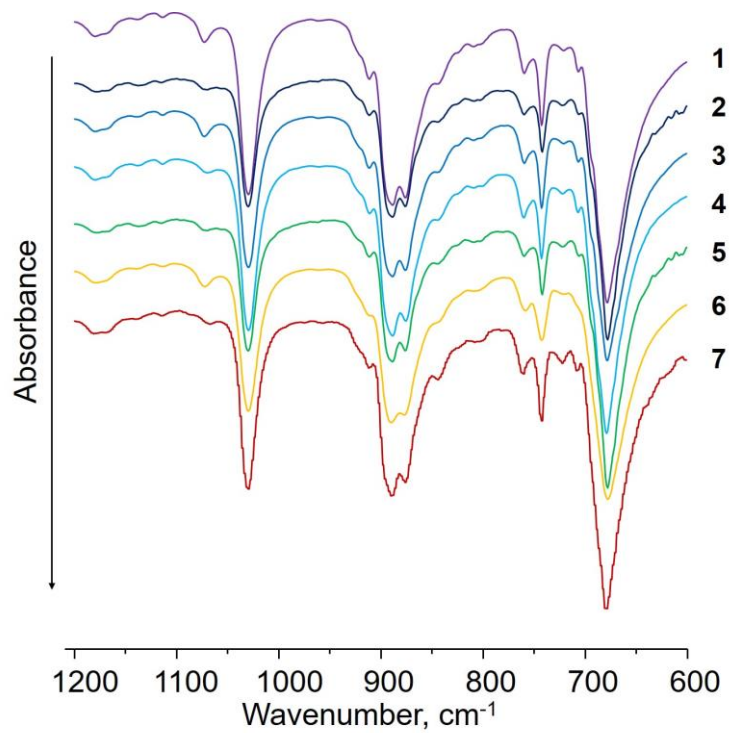


Fig. S1 ATR-IR spectra of **1-7**.

III. X-Ray Powder Diffraction and Le Bail Fit

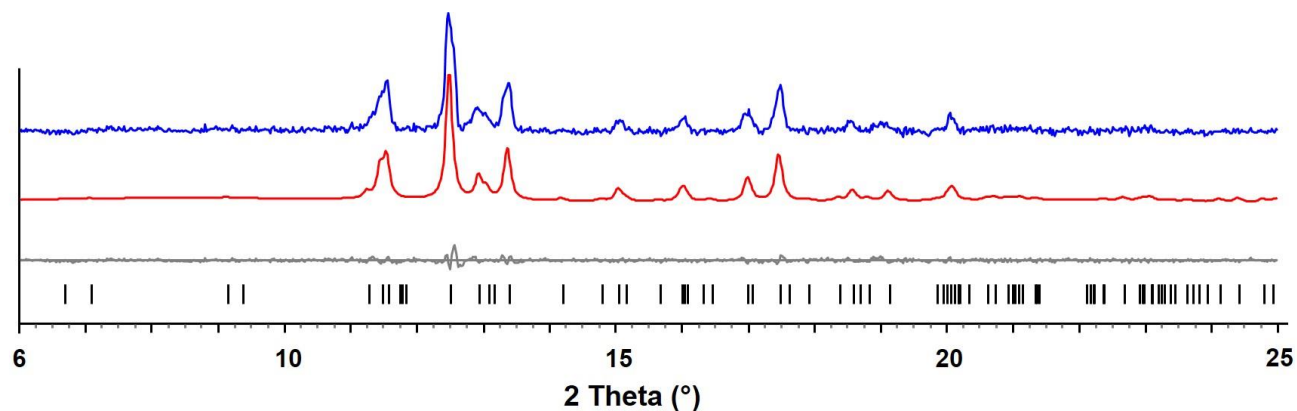


Fig. S2 X-ray powder diffraction pattern of **1-Gd** and Le Bail fit. The blue and red lines are experimental and calculated patterns, respectively. The grey line is the difference curve with theoretical positions shown at the bottom in black.

Table S1 Comparison of unit cell parameters for **1-Gd** from single crystal data and the Le Bail fit

1-Gd		
	Single crystal data (100 K)	Le Bail fit data (298 K)
Space Group	$P2_1/c$	
a (Å)	9.2772(3)	9.392(3)
b (Å)	13.9703(5)	14.079(2)
c (Å)	26.2056(9)	26.320(5)
α (°)	90	90
β (°)	90.079(1)	90.51(2)
γ (°)	90	90
V (Å ³)	3396.4(2)	3480.0(12)

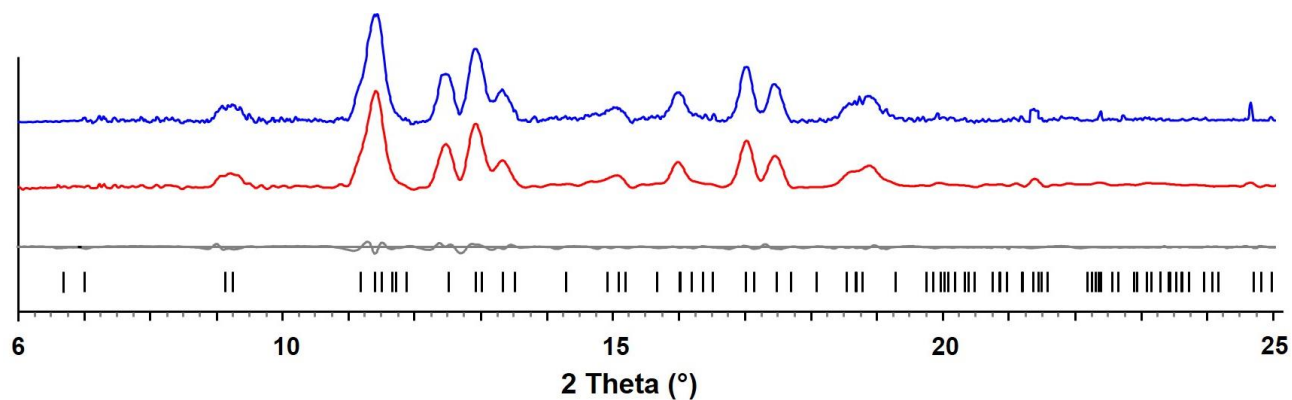


Fig. S3 X-ray powder diffraction pattern of **2-Tb** and Le Bail fit. The blue and red lines are experimental and calculated patterns, respectively. The grey line is the difference curve with theoretical positions shown at the bottom in black.

Table S2 Comparison of unit cell parameters for **2-Tb** from single crystal data and the Le Bail fit

2-Tb		
	Single crystal data (100 K)	Le Bail fit data (298 K)
Space Group	$P2_1/c$	
a (Å)	9.2738(6)	9.546(3)
b (Å)	13.9561(10)	14.271(9)
c (Å)	26.155(2)	25.571(9)
α (°)	90	90
β (°)	90.302(2)	90.76(2)
γ (°)	90	90
V (Å ³)	3385.1(4)	3619.7(2)

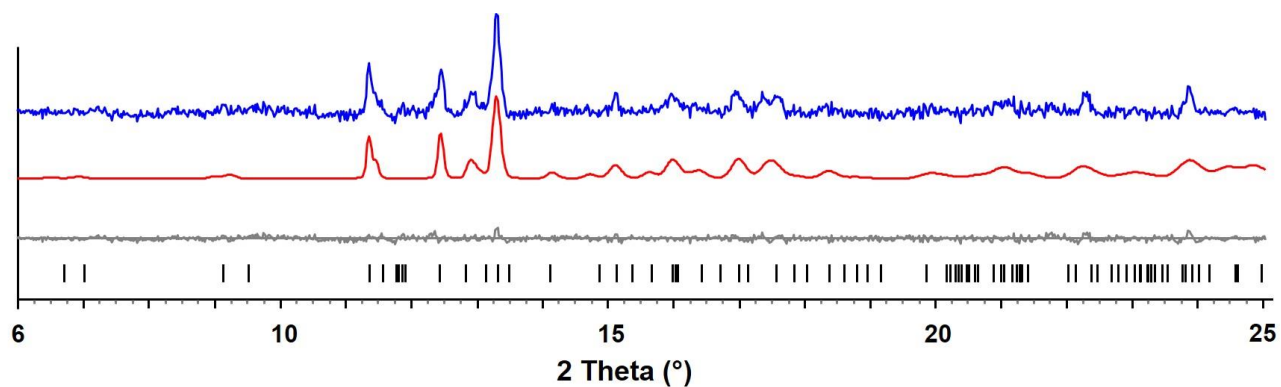


Fig. S4 X-ray powder diffraction pattern of **3-Dy** and Le Bail fit. The Blue and red lines are experimental and calculated patterns, respectively. The grey line is the difference curve with theoretical positions shown at the bottom in black.

Table S3 Comparison of unit cell parameters for **3-Dy** from single crystal data and the Le Bail fit

3-Dy		
	Single crystal data (100 K)	Le Bail fit data (298K)
Space Group	$P2_1/c$	
a (Å)	9.2628(5)	9.253(6)
b (Å)	13.9533(7)	14.235(4)
c (Å)	26.11417(13)	26.127(5)
α (°)	90	90
β (°)	90.377(2)	90.67(5)
γ (°)	90	90
V (Å ³)	3378.7(3)	3440.7(6)

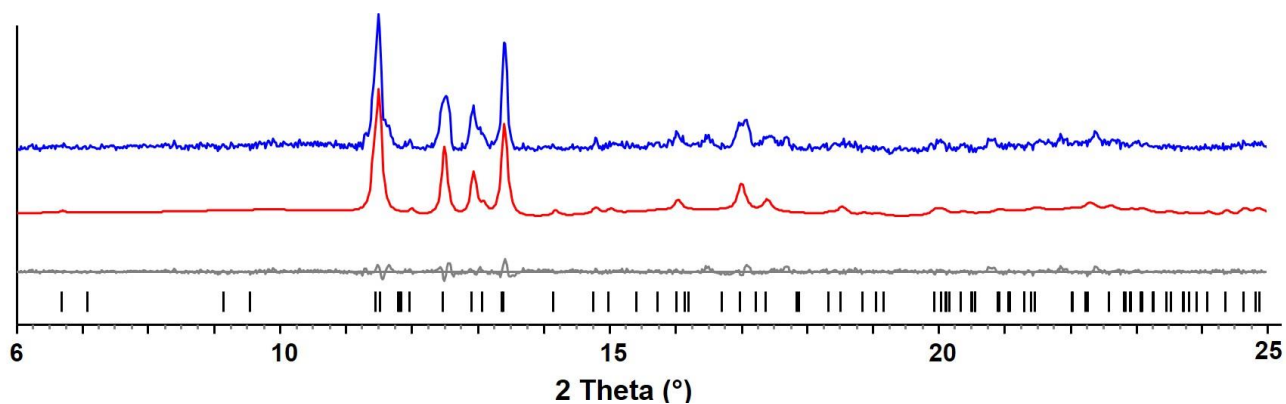


Fig. S5 X-ray powder diffraction pattern of **4-Ho** and Le Bail fit. The blue and red lines are experimental and calculated patterns, respectively. The grey line is the difference curve with theoretical positions shown at the bottom in black.

Table S4 Comparison of unit cell parameters for **4-Ho** from single crystal data and the Le Bail fit

4-Ho		
	Single crystal data (100 K)	Le Bail fit data (298 K)
Space Group	<i>P2₁/c</i>	
<i>a</i> (Å)	9.2613(3)	9.265(3)
<i>b</i> (Å)	13.9568(5)	14.190(3)
<i>c</i> (Å)	26.1226(10)	26.485(9)
α (°)	90	90
β (°)	90.566(2)	91.85(2)
γ (°)	90	90
<i>V</i> (Å ³)	3376.4(2)	3480.2(3)

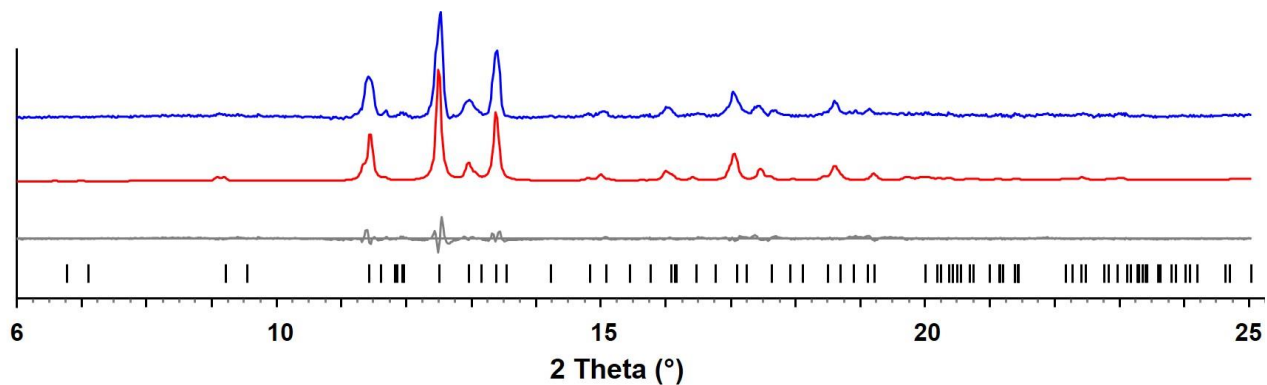


Fig. S6 X-ray powder diffraction pattern of **5-Er** and Le Bail fit. The blue and red lines are experimental and calculated patterns, respectively. The grey line is the difference curve with theoretical positions shown at the bottom in black.

Table S5 Comparison of unit cell parameters for **5-Er** from single crystal data and the Le Bail fit

5-Er		
	Single crystal data (100 K)	Le Bail fit data (298 K)
Space Group	<i>P2₁/c</i>	
<i>a</i> (Å)	9.2555(7)	9.251(6)
<i>b</i> (Å)	13.951(1)	14.150(1)
<i>c</i> (Å)	26.113(2)	26.092(6)
α (°)	90	90
β (°)	90.709(1)	91.12(5)
γ (°)	90	90
<i>V</i> (Å ³)	3371.6(4)	3415.0(5)

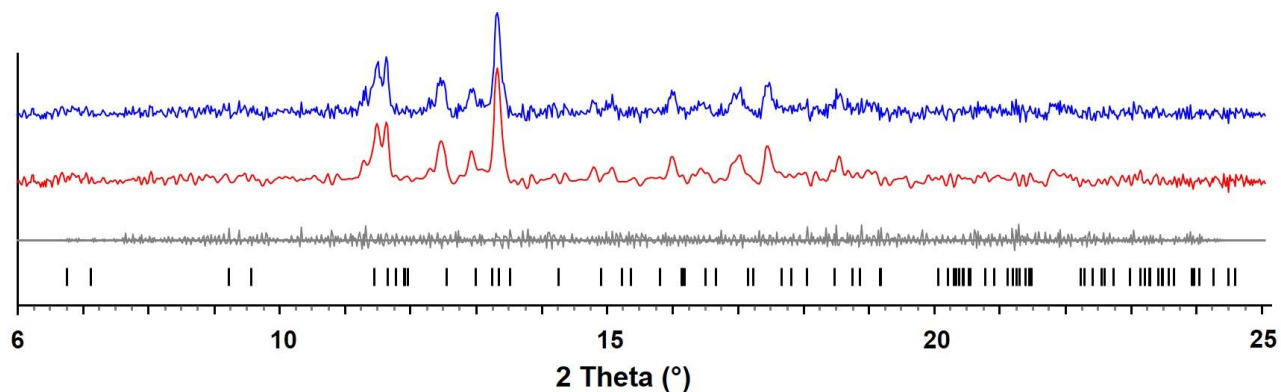


Fig. S7 X-ray powder diffraction pattern of **6-Tm** and Le Bail fit. The blue and red lines are experimental and calculated patterns, respectively. The grey line is the difference curve with theoretical positions shown at the bottom in black.

Table S6 Comparison of unit cell parameters for **6-Tm** from single crystal data and the Le Bail fit

6-Tm		
	Single crystal data (100 K)	Le Bail fit data (298 K)
Space Group	$P2_1/c$	
a (Å)	9.2730(7)	9.261(9)
b (Å)	13.9700(11)	14.11(4)
c (Å)	26.160(2)	26.21(2)
α (°)	90	90
β (°)	90.4780(10)	91.4(1)
γ (°)	90	90
V (Å ³)	3388.8(5)	3428.7(9)

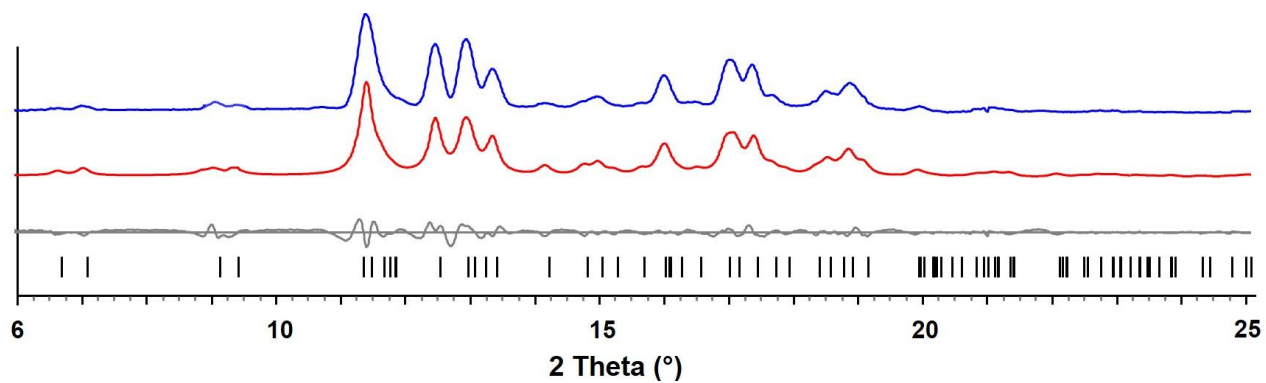


Fig. S8 X-ray powder diffraction pattern of **7-Yb** and Le Bail fit. The blue and red lines are experimental and calculated patterns, respectively. The grey line is the difference curve with theoretical positions shown at the bottom in black.

Table S7 Comparison of unit cell parameters for **7-Yb** from single crystal data and the Le Bail fit

7-Yb		
	Single crystal data (100 K)	Le Bail fit data (298 K)
Space Group	$P2_1/c$	
a (Å)	9.2730(7)	9.439(2)
b (Å)	13.9700(11)	14.203(3)
c (Å)	26.160(2)	26.553(7)
α (°)	90	90
β (°)	90.4780(10)	91.05(1)
γ (°)	90	90
V (Å ³)	3388.8(5)	3560.8(1)

IV. Crystal Structure Solution and Refinement Details

Data collections of **1–7** were performed on a Bruker D8 VENTURE X-ray diffractometer with PHOTON 100 CMOS shutterless mode detector equipped with a Mo-target X-ray tube ($\lambda = 0.71073 \text{ \AA}$) at $T = 100(2)$ K. Data reduction and integration were performed with the Bruker software package SAINT (version 8.38A).³ Data were corrected for absorption effects using the empirical methods as implemented in SADABS (version 2016/2).⁴ The structures were solved by SHELXT⁵ and refined by full-matrix least-squares procedures using the Bruker SHELXTL (version 2016/6)⁶ software package. All non-hydrogen atoms (including those in disordered parts) were refined anisotropically. The H atoms were also included at calculated positions and refined as riders, with $U_{\text{iso}}(\text{H}) = 1.2 U_{\text{eq}}(\text{C})$. Crystallographic data for **1–7** and details of the data collection and structure refinement are listed in Table S8.

Table S8 Crystal data and structure refinement parameters for **1–7**

Compound	1-Gd	2-Tb	3-Dy	4-Ho
Empirical formula	C ₃₆ H ₄₈ CaGdKO ₃	C ₃₆ H ₄₈ CaTbKO ₃	C ₃₆ H ₄₈ CaDyKO ₃	C ₃₆ H ₄₈ CaHoKO ₃
Formula weight	765.17	766.84	770.42	772.85
Temperature (K)	100(2)	100(2)	100(2)	100(2)
Wavelength (Å)	0.71073	0.71073	0.71073	0.71073
Crystal system	Monoclinic	Monoclinic	Monoclinic	Monoclinic
Space group	<i>P2₁/c</i>	<i>P2₁/c</i>	<i>P2₁/c</i>	<i>P2₁/c</i>
<i>a</i> (Å)	9.2772(3)	9.2738(6)	9.2628(5)	9.2613(3)
<i>b</i> (Å)	13.9703(5)	13.9561(10)	13.9533(7)	13.9568(5)
<i>c</i> (Å)	26.2056(9)	26.1550(18)	26.1417(13)	26.1226(10)
α (°)	90.00	90.00	90.00	90.00
β (°)	90.0790(10)	90.302(2)	90.377(2)	90.566(2)
γ (°)	90.00	90.00	90.00	90.00
<i>V</i> (Å ³)	3396.4(2)	3385.1(4)	3378.7(3)	3376.4(2)
<i>Z</i>	4	4	4	4
ρ_{calcd} (g·cm ⁻³)	1.496	1.505	1.515	1.520
μ (mm ⁻¹)	2.259	2.397	2.520	2.652
<i>F</i> (000)	1564	1568	1572	1576
Crystal size (mm)	0.03×0.17×0.52	0.10×0.15×0.48	0.04×0.15×0.39	0.05×0.07×0.21
θ range for data collection (°)	2.75-33.79	3.02-43.20	2.75-25.05	2.75-30.57
Reflections collected	95537	191623	74320	135796
Independent reflections	13580	25203	5954	10339
	[<i>R</i> _{int} = 0.0591]	[<i>R</i> _{int} = 0.0754]	[<i>R</i> _{int} = 0.0885]	[<i>R</i> _{int} = 0.0630]
Transmission factors (min/max)	0.5352/0.7467	0.7320/0.8456	0.7730/0.8653	0.7940/0.8992
Data/restraints/params.	13580/0/379	25203/0/379	5954/849/373	10339/0/379
<i>R</i> 1, ^a <i>wR</i> 2 ^b (<i>I</i> > 2 σ (<i>I</i>))	0.0457, 0.0617	0.0424, 0.0933	0.0584, 0.1247	0.0333, 0.0545
<i>R</i> 1, ^a <i>wR</i> 2 ^b (all data)	0.0710, 0.0673	0.0541, 0.0980	0.0727, 0.1313	0.0477, 0.0578
Quality-of-fit ^c	1.094	1.108	1.141	1.090

Compound	5-Er	6-Tm	7-Yb
Empirical formula	C ₃₆ H ₄₈ CaErKO ₃	C ₃₆ H ₄₈ CaTmKO ₃	C ₃₆ H ₄₈ CaYbKO ₃
Formula weight	775.18	776.85	780.96
Temperature (K)	100(2)	100(2)	100(2)
Wavelength (Å)	0.71073	0.71073	0.71073
Crystal system	Monoclinic	Monoclinic	Monoclinic
Space group	<i>P</i> 2 ₁ / <i>c</i>	<i>P</i> 2 ₁ / <i>c</i>	<i>P</i> 2 ₁ / <i>c</i>
<i>a</i> (Å)	9.2555(7)	9.2649(8)	9.2602(7)
<i>b</i> (Å)	13.9514(11)	13.9648(11)	13.9561(10)
<i>c</i> (Å)	26.113(2)	26.111(2)	26.1046(19)
α (°)	90.00	90.00	90.00
β (°)	90.7090(10)	90.8583(15)	90.935(2)
γ (°)	90.00	90.00	90.00
<i>V</i> (Å ³)	3371.6(4)	3377.9(5)	3373.2(4)
<i>Z</i>	4	4	4
ρ_{calcd} (g·cm ⁻³)	1.527	1.528	1.538
μ (mm ⁻¹)	2.798	2.935	3.081
<i>F</i> (000)	1580	1584	2084
Crystal size (mm)	0.05×0.08×0.24	0.03×0.17×0.32	0.04×0.15×0.52
θ range for data collection (°)	2.75-35.08	2.76-37.87	2.74-37.10
Reflections collected	197098	108685	88786
Independent reflections	14885	17902	16802
	[<i>R</i> _{int} = 0.0712]	[<i>R</i> _{int} = 0.0415]	[<i>R</i> _{int} = 0.0428]
Transmission factors (min/max)	0.6938/0.7569	0.4232/0.7474	0.6648/0.7896
Data/restraints/params.	14885/0/379	17902/0/379	16802/0/379
<i>R</i> 1, ^a <i>wR</i> 2 ^b (<i>I</i> > 2 σ (<i>I</i>))	0.0339, 0.0508	0.0385, 0.0707	0.0363, 0.0493
<i>R</i> 1, ^a <i>wR</i> 2 ^b (all data)	0.0495, 0.0542	0.0550, 0.0753	0.0564, 0.0530
Quality-of-fit ^c	1.094	1.129	1.073

^a*R*1 = $\sum ||F_o| - |F_c|| / \sum |F_o|$. ^b*wR*2 = $[\sum [w(F_o^2 - F_c^2)^2] / \sum [w(F_o^2)^2]]^{1/2}$.

^cQuality-of-fit *S* = $[\sum [w(F_o^2 - F_c^2)^2] / (N_{\text{obs}} - N_{\text{params}})]^{1/2}$, based on all data.

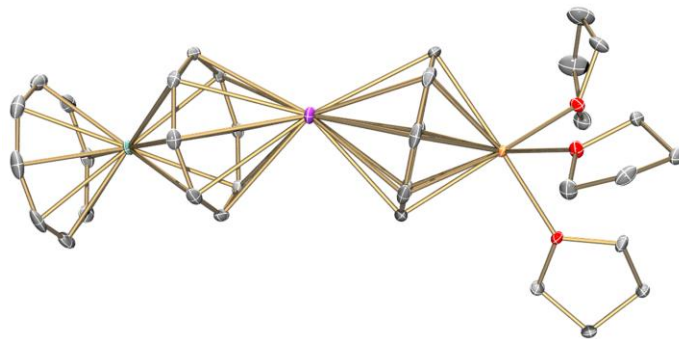


Fig. S9 ORTEP drawing of **1-Gd**, drawn with thermal ellipsoids at the 40% probability level. All hydrogen atoms are removed for clarity. The color scheme used: C grey, O red, K dark orchid, Ca orange, Gd green copper.

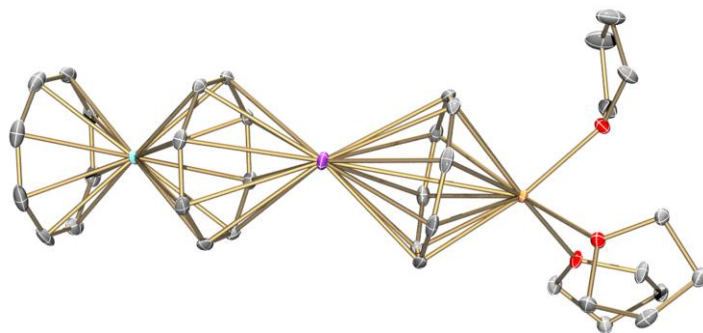


Fig. S10 ORTEP drawing of **2-Tb**, drawn with thermal ellipsoids at the 40% probability level. All hydrogen atoms are removed for clarity. The color scheme used: C grey, O red, K dark orchid, Ca orange, Tb medium turquoise.

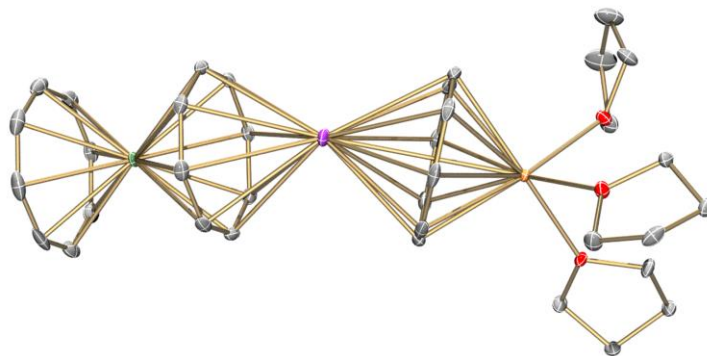


Fig. S11 ORTEP drawing of **3-Dy**, drawn with thermal ellipsoids at the 40% probability level. All hydrogen atoms are removed for clarity. The color scheme used: C grey, O red, K dark orchid, Ca orange, Dy medium sea green.

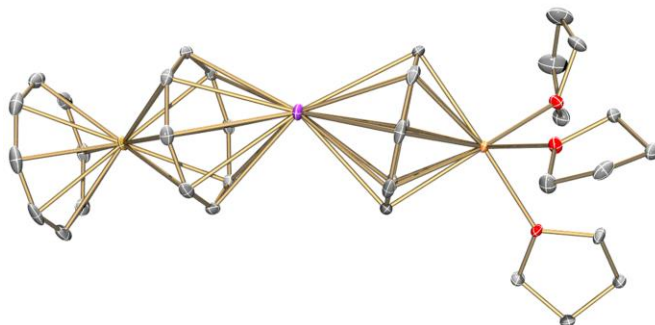


Fig. S12 ORTEP drawing of **4-Ho**, drawn with thermal ellipsoids at the 40% probability level. All hydrogen atoms are removed for clarity. The color scheme used: C grey, O red, K dark orchid, Ca orange, Ho sienna.

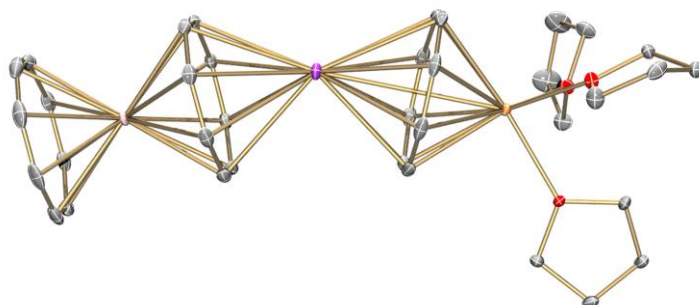


Fig. S13 ORTEP drawing of **5-Er**, drawn with thermal ellipsoids at the 40% probability level. All hydrogen atoms are removed for clarity. The color scheme used: C grey, O red, K dark orchid, Ca orange, Er pink.

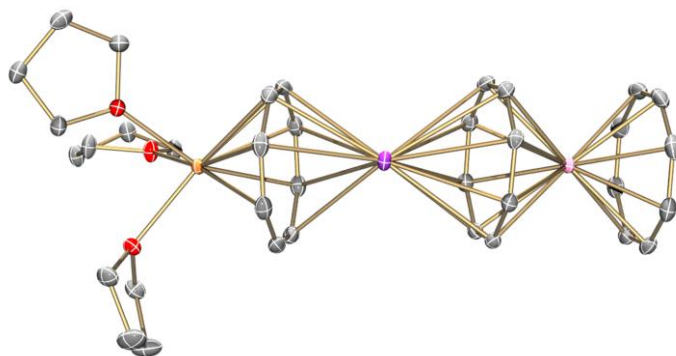


Fig. S14 ORTEP drawing of **6-Tm**, drawn with thermal ellipsoids at the 40% probability level. All hydrogen atoms are removed for clarity. The color scheme used: C grey, O red, K dark orchid, Ca orange, Tm medium violet.

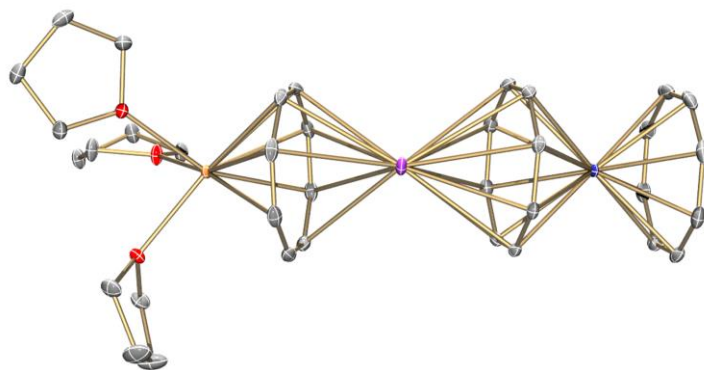


Fig. S15 ORTEP drawing of **7-Yb**, drawn with thermal ellipsoids at the 40% probability level. All hydrogen atoms are removed for clarity. The color scheme used: C grey, O red, K dark orchid, Ca orange, Yb navy blue.

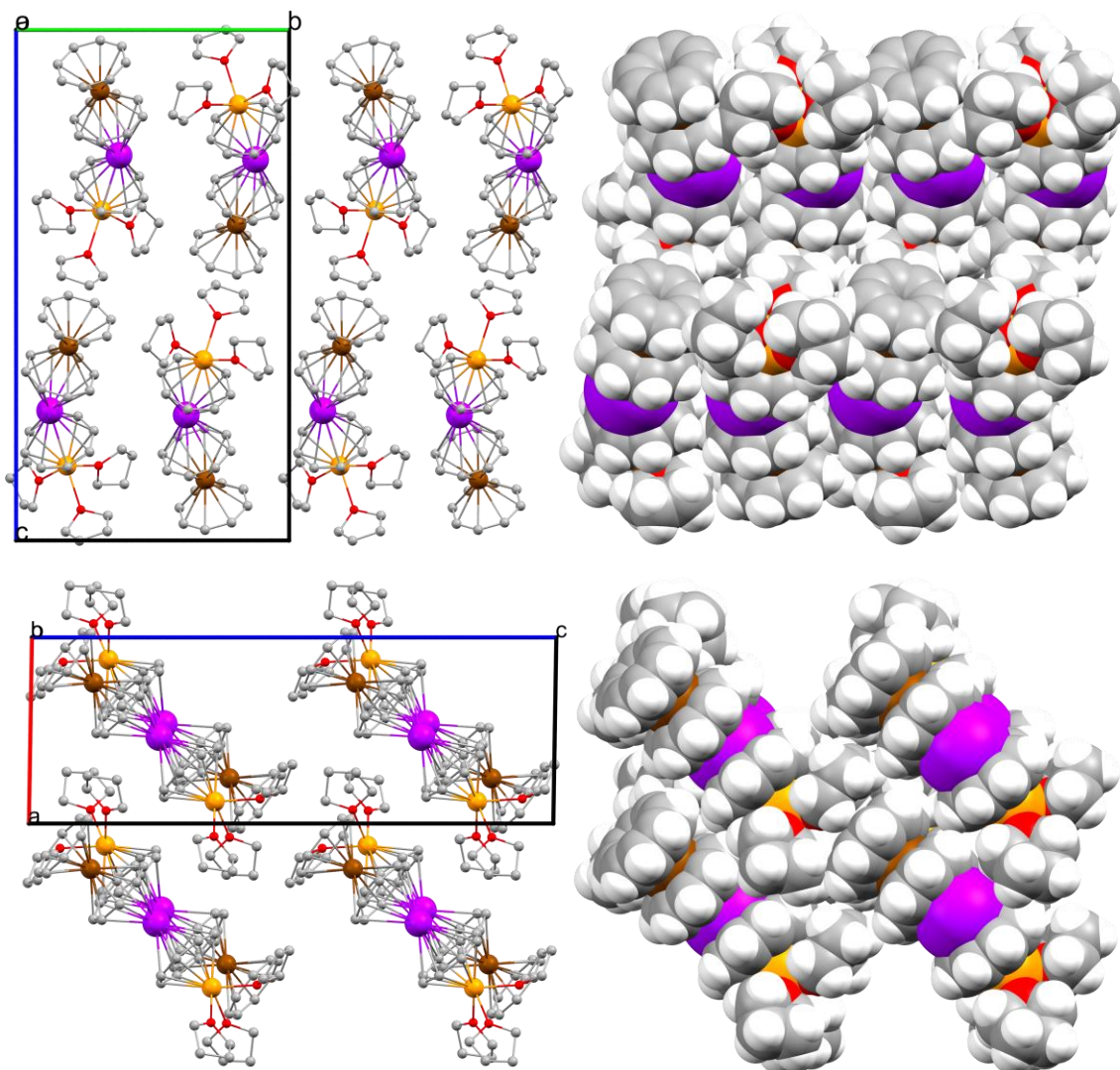
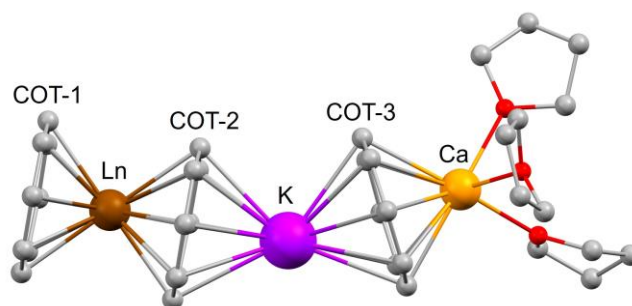


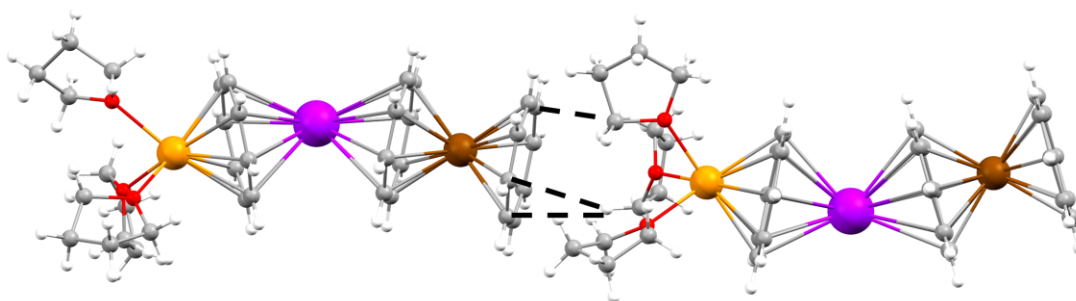
Fig. S16 Solid-state packing of **1-7**, ball-and-stick (no H-atoms) and space-filling models.

Table S9 Selected bond length distances (Å) in **1–7** along with a labeling scheme

	1-Gd	2-Tb	3-Dy	4-Ho	5-Er	6-Tm	7-Yb
Ln–C _{COT1, avg}	2.653(3)	2.640(2)	2.623(8)	2.615(3)	2.606(2)	2.599(2)	2.593(2)
Ln to centroid _{COT1}	1.913(3)	1.891(2)	1.874(8)	1.859(3)	1.846(2)	1.832(2)	1.827(2)
Ln–C _{COT2, avg}	2.691(3)	2.677(2)	2.662(8)	2.651(3)	2.644(2)	2.637(2)	2.614(2)
Ln to centroid _{COT2}	1.961(3)	1.939(2)	1.923(8)	1.907(3)	1.896(2)	1.881(2)	1.871(2)
K–C _{COT2, avg}	3.089(3)	3.089(2)	3.088(8)	3.086(3)	3.086(2)	3.089(2)	3.089(2)
K to centroid _{COT2}	2.479(3)	2.476(2)	2.478(8)	2.476(3)	2.475(2)	2.476(2)	2.478(2)
K–C _{COT3, avg}	3.032(3)	3.032(2)	3.030(8)	3.030(3)	3.031(2)	3.034(2)	3.032(2)
K to centroid _{COT3}	2.409(3)	2.407(2)	2.408(8)	2.407(3)	2.408(2)	2.409(2)	2.407(2)
Ca–C _{COT3, avg}	2.655(2)	2.658(2)	2.653(8)	2.656(2)	2.656(2)	2.658(2)	2.657(2)
Ca to centroid _{COT3}	1.915(2)	1.914(2)	1.912(8)	1.914(2)	1.913(2)	1.916(2)	1.913(2)
Ca–O _{THF, avg}	2.383(2)	2.383(1)	2.382(5)	2.382(2)	2.381(2)	2.384(2)	2.383(1)

Table S10 Selected dihedral angles (°) in **1–7**

	1-Gd	2-Tb	3-Dy	4-Ho	5-Er	6-Tm	7-Yb
COT1/COT2	0.77(9)	0.85(6)	0.90(3)	0.84(9)	0.81(7)	0.83(6)	0.89(6)
COT2/COT3	27.61(9)	27.45(6)	27.60(3)	27.47(9)	27.41(7)	27.33(6)	27.35(6)

Table S11 C–H··· π interactions (Å) in **1–7** along with a labeling scheme

	1-Gd	2-Tb	3-Dy	4-Ho	5-Er	6-Tm	7-Yb
C–H··· π	2.721(2)–	2.708(1)–	2.708(5)–	2.702(2)–	2.693(2)–	2.697(3)–	2.692(1)–
interaction	2.747(2)	2.732(1)	2.751(5)	2.729(2)	2.731(2)	2.725(3)	2.728(1)

Table S12 Selected M–M distances (Å) in **1–7**

	1-Gd	2-Tb	3-Dy	4-Ho	5-Er	6-Tm	7-Yb
Intermolecular Ln–Ln	9.277(2)	9.274(2)	9.263(2)	9.261(2)	9.255(2)	9.265(2)	9.260(2)
Intramolecular Ln–K	4.440(2)	4.414(2)	4.400(2)	4.383(2)	4.369(2)	4.356(2)	4.348(2)
Intramolecular Ca–K	4.323(2)	4.320(2)	4.319(2)	4.321(2)	4.320(2)	4.323(2)	4.319(2)

V. Magnetic Properties

Magnetic susceptibility measurements were performed on a Quantum Design SQUID MPMS-XL magnetometer and PPMS-II susceptometer housed at the Centre de Recherche Paul Pascal at temperatures between 1.8 and 400 K and *dc* magnetic fields ranging from -7 to +7 T. The *ac* magnetic susceptibility measurements were performed in an oscillating *ac* field of 1 to 6 Oe with frequencies between 10 and 10000 Hz in zero *dc*-field. The measurements were carried out on polycrystalline samples (3.3 for **1-Gd**, 4.5 mg for **2-Tb**, 3.1, 6.8, 4.9 mg for **3-Dy**, 2.7 mg for **4-Ho**, 10.5 mg for **5-Er** and 6.0 mg for **6-Tm**) suspended in mineral oil (typically 5-20 mg) and introduced in a sealed polyethene bag ($3 \times 0.5 \times 0.02$ cm; typically, 20-40 mg) in a glovebox a controlled atmosphere of nitrogen or argon. Prior to the experiments, the field-dependent magnetisation was measured at 100 K on each sample in order to detect the presence of any bulk ferromagnetic impurities. As expected for paramagnetic or diamagnetic materials, a perfectly linear dependence of the magnetisation that extrapolates to zero at zero *dc* field was systematically observed; the samples appeared to be free of any ferromagnetic impurities. The magnetic susceptibilities were corrected for the sample holder, the mineral oil and the intrinsic diamagnetic contributions.

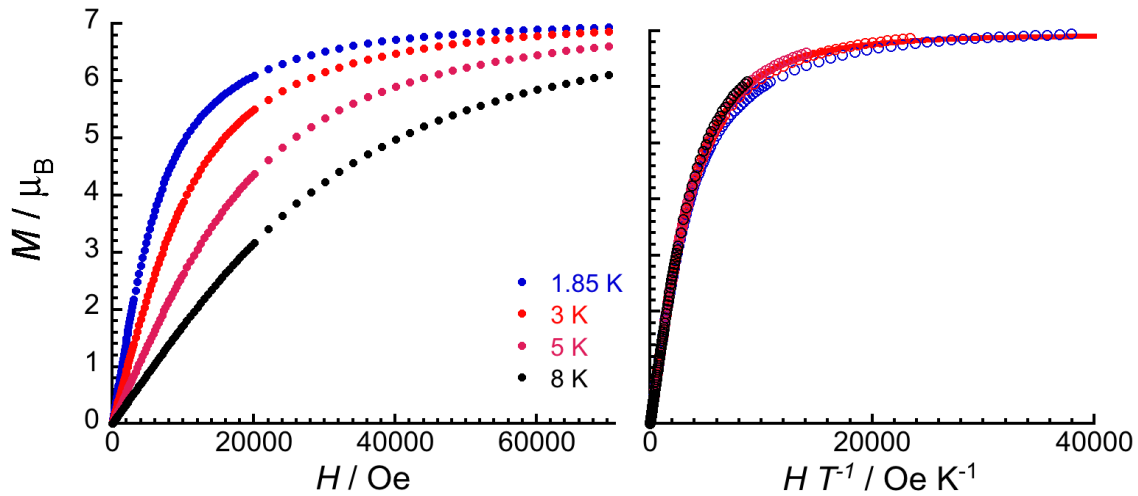


Fig. S17 Field dependence of the magnetisation for **1-Gd** at low temperatures between 1.85 and 8 K with applied magnetic field from 0 to 7 T. The magnetization data are shown as a M versus H plot on the left and as a M versus H/T plot on the right (field sweeping rates: 80 Oe/min between 0 and 0.1 T, 170 Oe/min between 0.1 and 0.3 T, 400 Oe/min between 0.3 and 1 T, 830 Oe/min between 1 and 2 T, 2800 Oe/min between 2 and 7 T). At 1.85 K and 7 T, the magnetization reaches a value of $6.94 \mu_B$. The solid red line is the best fit of the experimental M versus H/T data to the $S = 7/2$ Brillouin function with $g = 1.98(3)$.

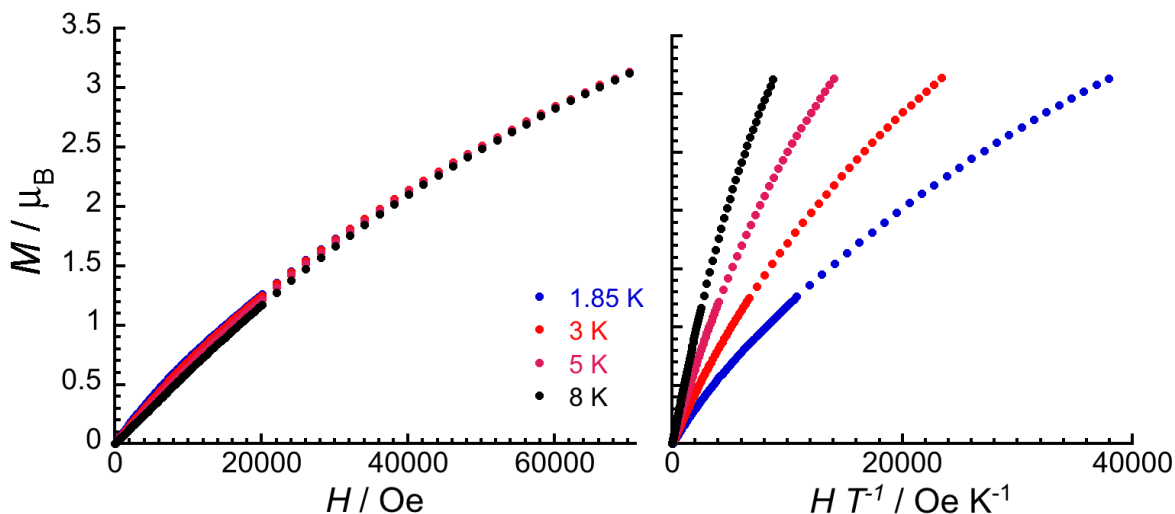


Fig. S18 Field dependence of the magnetisation for **2-Tb** at low temperatures between 1.85 and 8 K with applied magnetic field from 0 to 7 T. The magnetization data are shown as a M versus H plot on the left and as a M versus H/T plot on the right (field sweeping rates: 80 Oe/min between 0 and 0.1 T, 170 Oe/min between 0.1 and 0.3 T, 400 Oe/min between 0.3 and 1 T, 830 Oe/min between 1 and 2 T, 2800 Oe/min between 2 and 7 T). At 1.85 K and 7 T, the magnetization reaches a value of $3.13 \mu_B$.

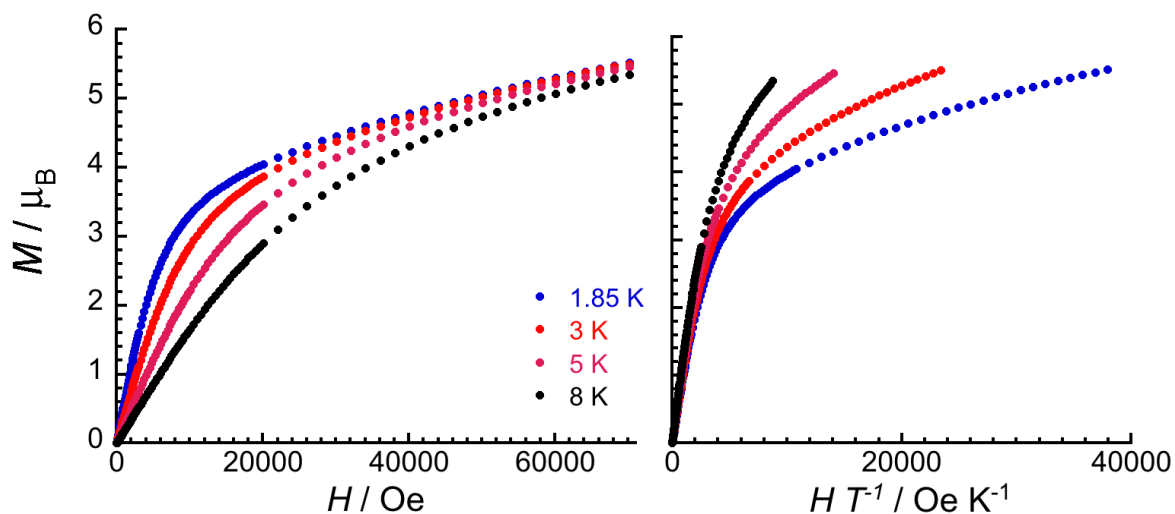


Fig. S19 Field dependence of the magnetisation for **3-Dy** at low temperatures between 1.85 and 8 K with applied magnetic field from 0 to 7 T. The magnetization data are shown as a M versus H plot on the left and as a M versus H/T plot on the right (field sweeping rates: 80 Oe/min between 0 and 0.1 T, 170 Oe/min between 0.1 and 0.3 T, 400 Oe/min between 0.3 and 1 T, 830 Oe/min between 1 and 2 T, 2800 Oe/min between 2 and 7 T). At 1.85 K and 7 T, the magnetization reaches a value of $5.52 \mu_B$.

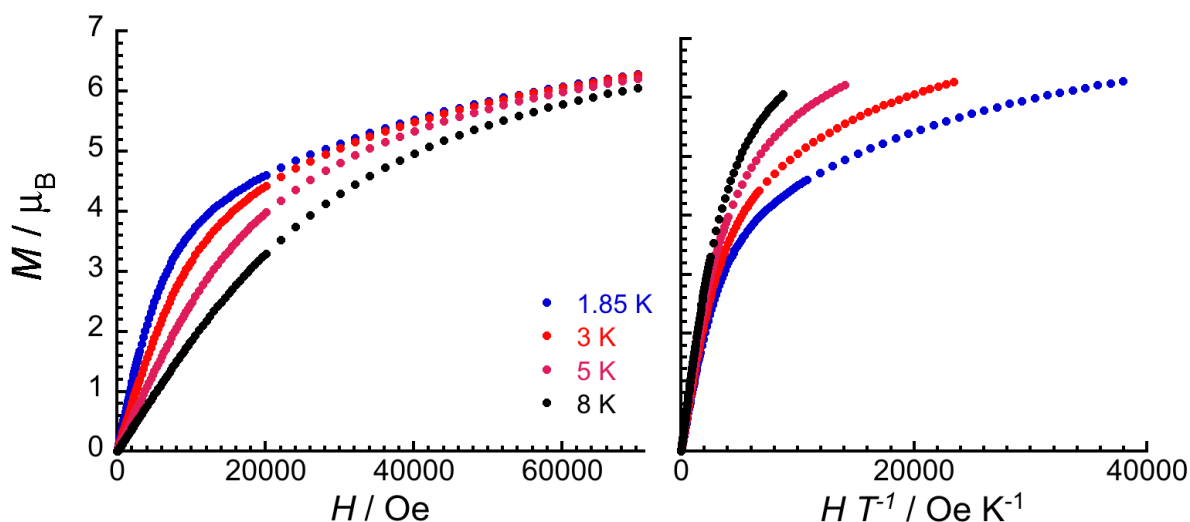


Fig. S20 Field dependence of the magnetisation for **4-Ho** at low temperatures between 1.85 and 8 K with applied magnetic field from 0 to 7 T. The magnetization data are shown as a M versus H plot on the left and as a M versus H/T plot on the right (field sweeping rates: 80 Oe/min between 0 and 0.1 T, 170 Oe/min between 0.1 and 0.3 T, 400 Oe/min between 0.3 and 1 T, 830 Oe/min between 1 and 2 T, 2800 Oe/min between 2 and 7 T). At 1.85 K and 7 T, the magnetization reaches a value of $6.28 \mu_B$.

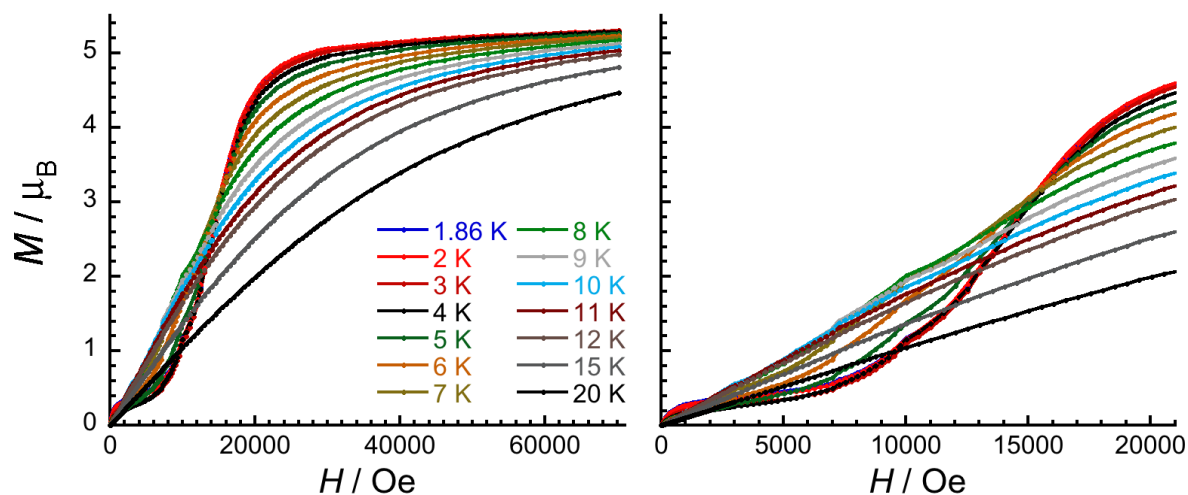


Fig. S21 Field dependence of the magnetisation for **5-Er** at low temperatures between 1.85 and 8 K with applied magnetic field from 0 to 7 T (after a zero-field cooling from 20 K). The M versus H data are shown on full scale from 0 to 7 T on the left and between 0 and 2.1 T on the right (field sweeping rates: 80 Oe/min between 0 and 0.1 T, 170 Oe/min between 0.1 and 0.3 T, 400 Oe/min between 0.3 and 1 T, 830 Oe/min between 1 and 3 T, 2800 Oe/min between 3 and 7 T). At 1.85 K and 7 T, the magnetization reaches a value of $5.29 \mu_B$.

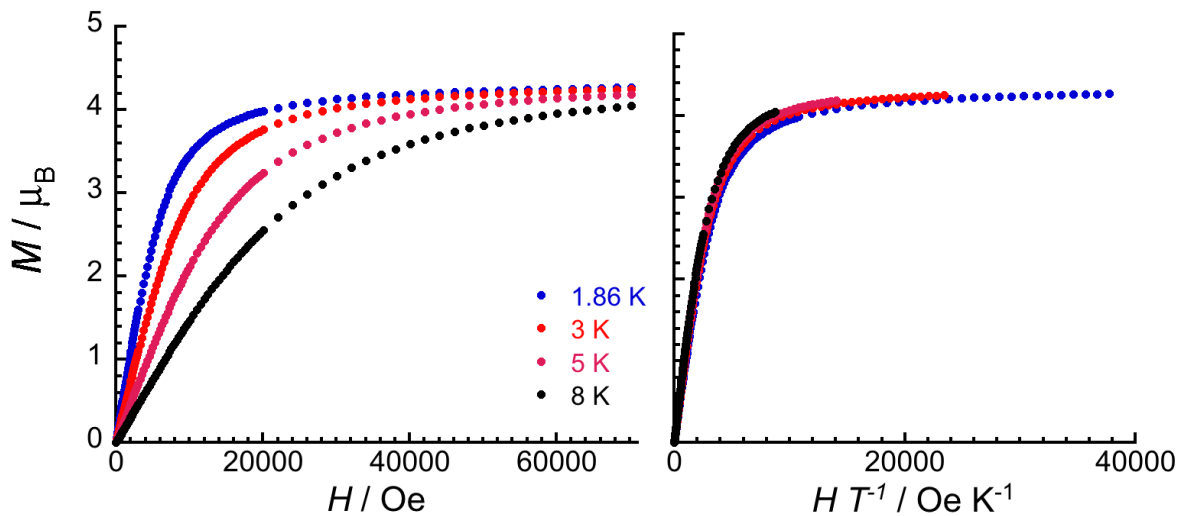


Fig. S22 Field dependence of the magnetisation for **6-Tm** at low temperatures between 1.85 and 8 K with applied magnetic field from 0 to 7 T. The magnetization data are shown as a M versus H plot on the left and as a M versus H/T plot on the right (field sweeping rates: 80 Oe/min between 0 and 0.1 T, 170 Oe/min between 0.1 and 0.3 T, 400 Oe/min between 0.3 and 1 T, 830 Oe/min between 1 and 2 T, 2800 Oe/min between 2 and 7 T). At 1.85 K and 7 T, the magnetization reaches a value of 4.27 μ_B .

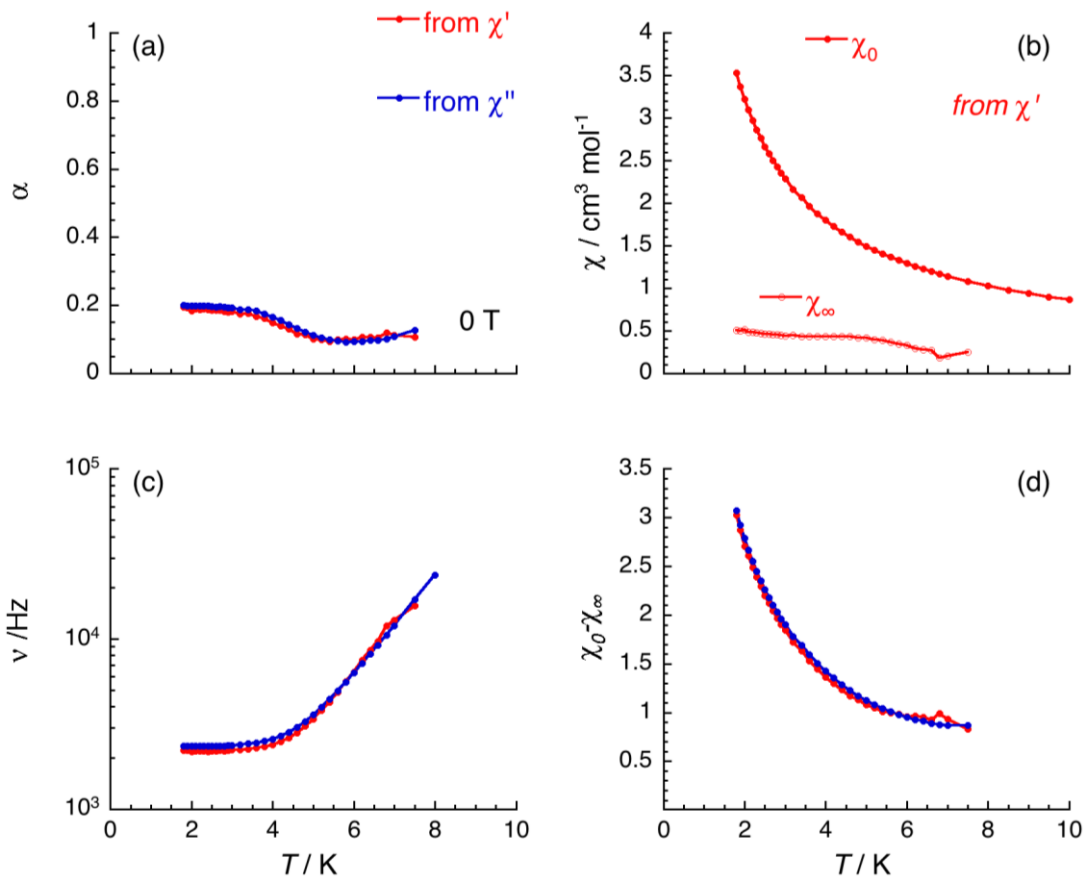


Fig. S23 Temperature dependence of the parameters α , ν , χ_0 , χ_∞ and $\chi_0 - \chi_\infty$, between 1.85 and 8 K in zero-field deduced from the generalised Debye fit of the frequency dependence of the real (χ') and imaginary (χ'') components of the ac susceptibility shown in Fig. 7 (main text), for **3-Dy**.

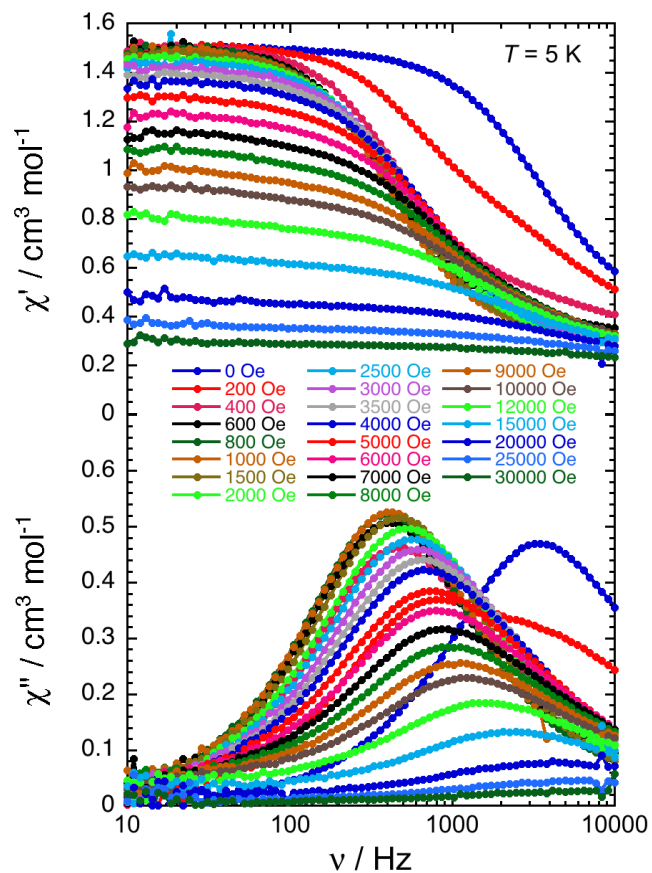


Fig. S24 ac frequency dependences (between 0.1 and 10000 Hz) of the real (χ' , top) and imaginary (χ'' , bottom) parts of the ac susceptibility for **3-Dy** at 5 K and under an applied dc field varying between 0 and 3 T. The solid lines are guides for the eyes.

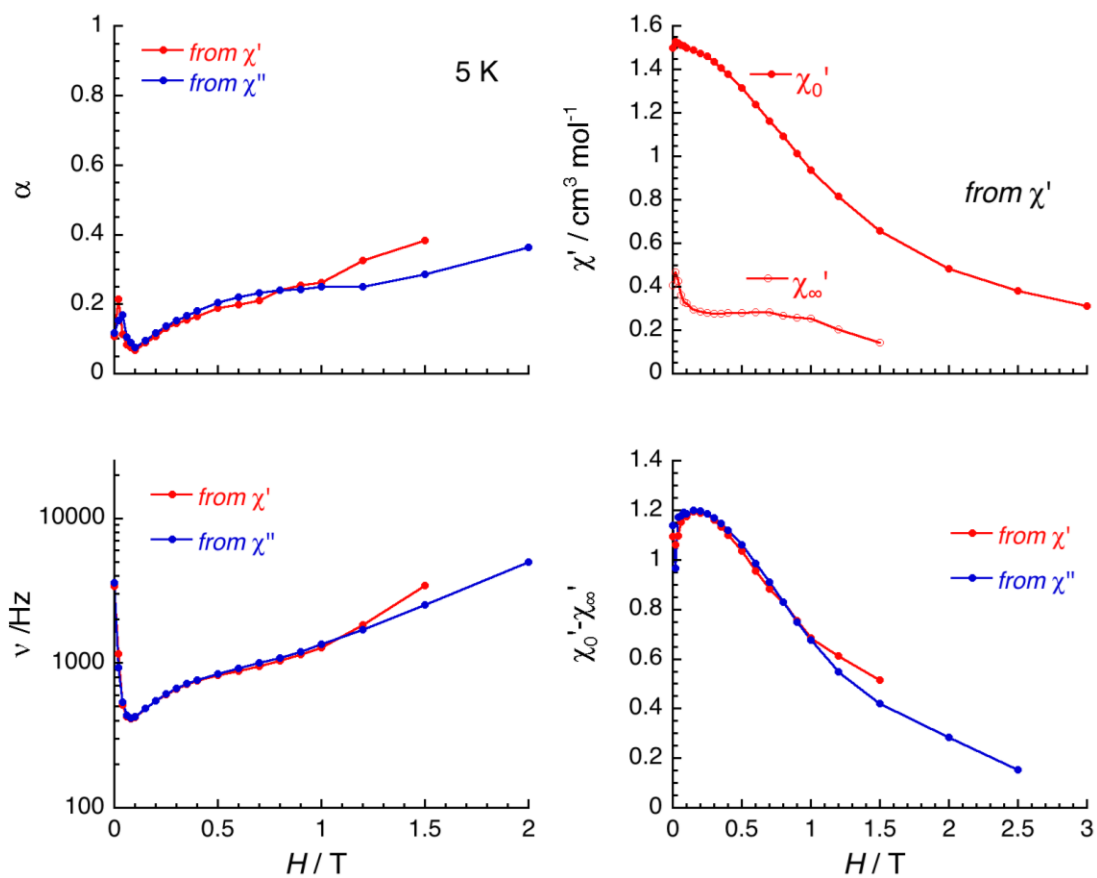


Fig. S25 Field dependence of the parameters α , ν , χ_0 , χ_∞ and $\chi_0 - \chi_\infty$, between 0 and 2 T at 5 K deduced from the generalised Debye fit of the frequency dependence of the real (χ') and imaginary (χ'') components of the ac susceptibility shown in the above Fig. S24, for **3-Dy**.

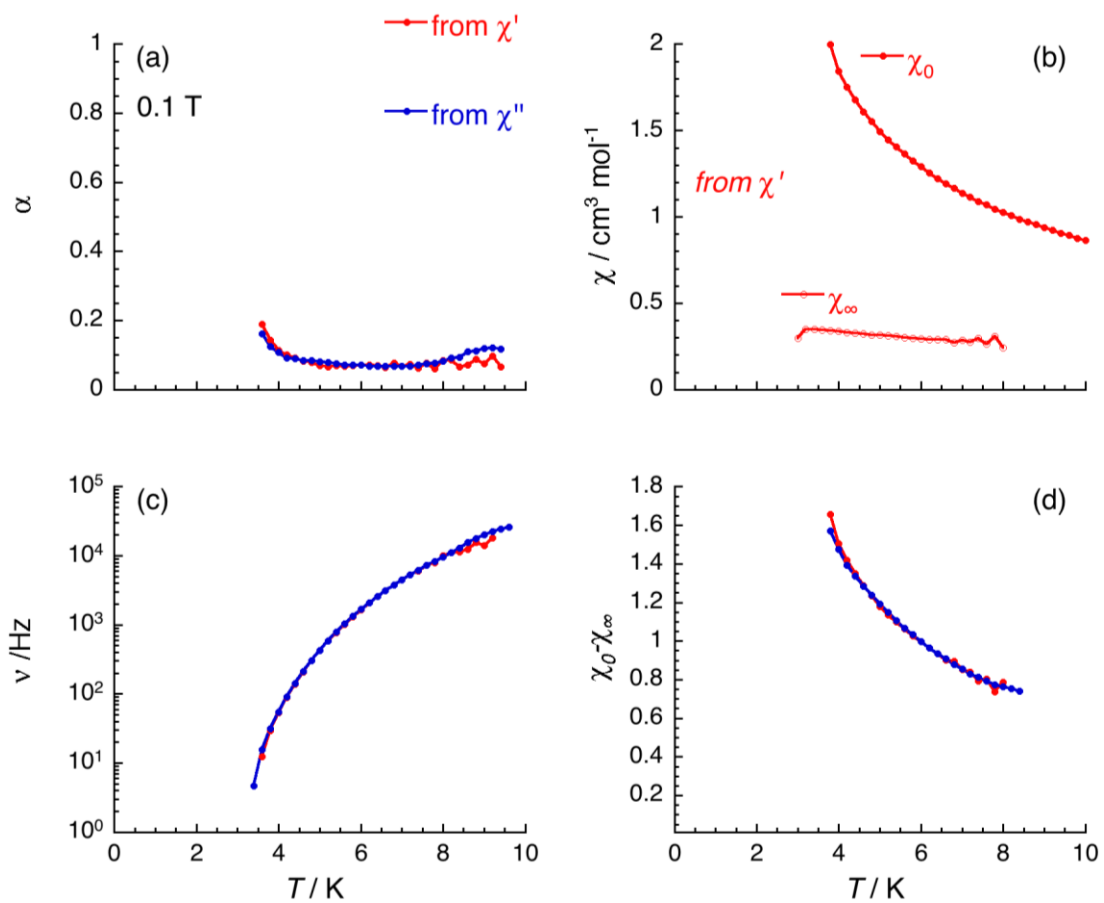


Fig. S26 Temperature dependence of the parameters α , ν , χ_0 , χ_∞ and $\chi_0 - \chi_\infty$, between 3.4 and 9.2 K under an applied dc field of 0.1 T, deduced from the generalised Debye fit of the frequency dependence of the real (χ') and imaginary (χ'') components of the ac susceptibility shown in Fig. 8 (main text), for **3-Dy**.

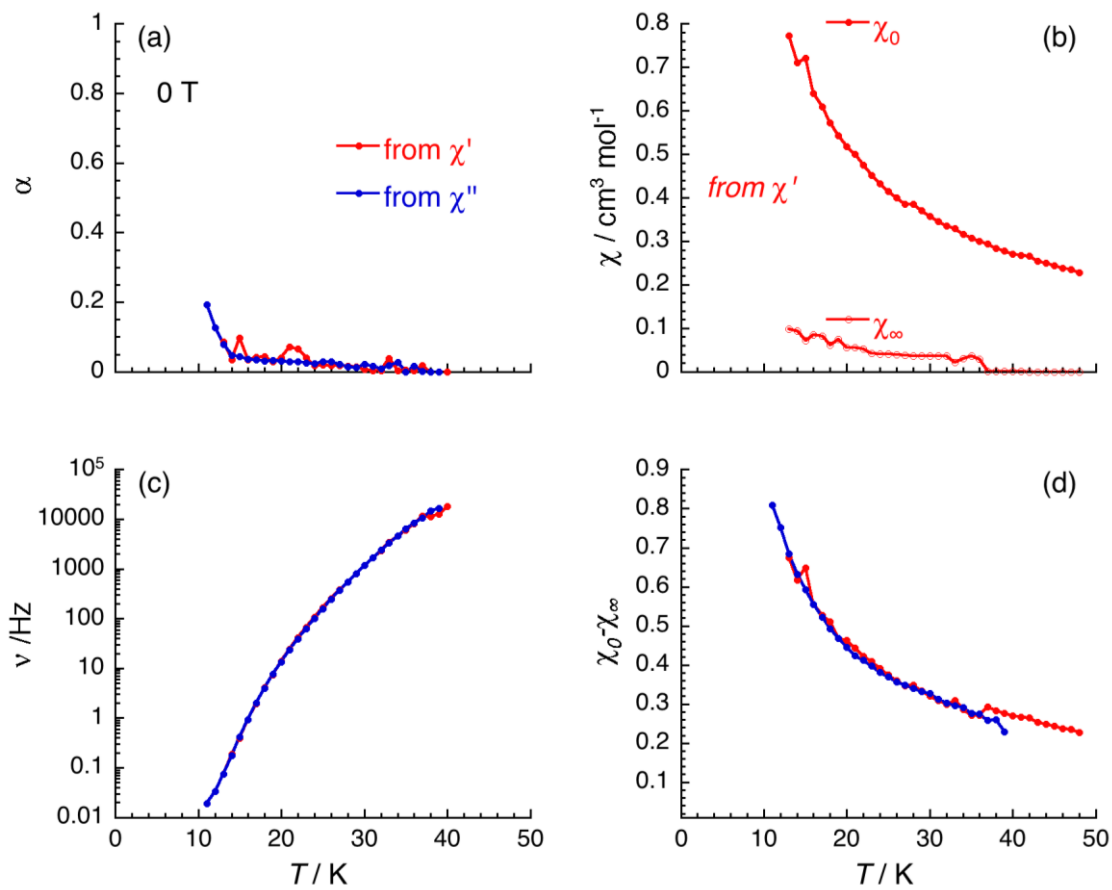


Fig. S27 Temperature dependence of the parameters α , ν , χ_0 , χ_∞ and $\chi_0 - \chi_\infty$, between 1.85 and 8 K in zero-field deduced from the generalised Debye fit of the frequency dependence of the real (χ') and imaginary (χ'') components of the ac susceptibility shown in Fig. 10 (main text), for **5-Er**.

The relaxation rate, τ^{-1} , of a given system can thus be summarized by the following equations:

$$\tau^{-1} = \tau_{Raman}^{-1} + \tau_{Direct}^{-1} + \tau_{Orbach}^{-1} + \tau_{QTM}^{-1} \quad (1)$$

$$\tau^{-1} = C \frac{1 + C_1 H^2}{1 + C_2 H^2} T^n + A T H^4 + \tau_0^{-1} \exp\left(-\frac{\Delta \left(1 - \frac{H}{H_0}\right)^m}{k_B T}\right) + \frac{B_1}{1 + B_2 H^2} \quad (2)$$

Equation 2 shows that these four processes have their own temperature (T) and field (H) dependence, which rely on a eleven parameters (A , n , B_1 , B_2 , C , C_1 , C_2 , Δ , τ_0 , m and H_0 ; with for the Orbach-like relaxation, Δ being the energy barrier at zero applied field, H_0 the reversal field at zero temperature, τ_0 the attempt relaxation time and m a constant of the order of the unity usually between 1.5 and 2).

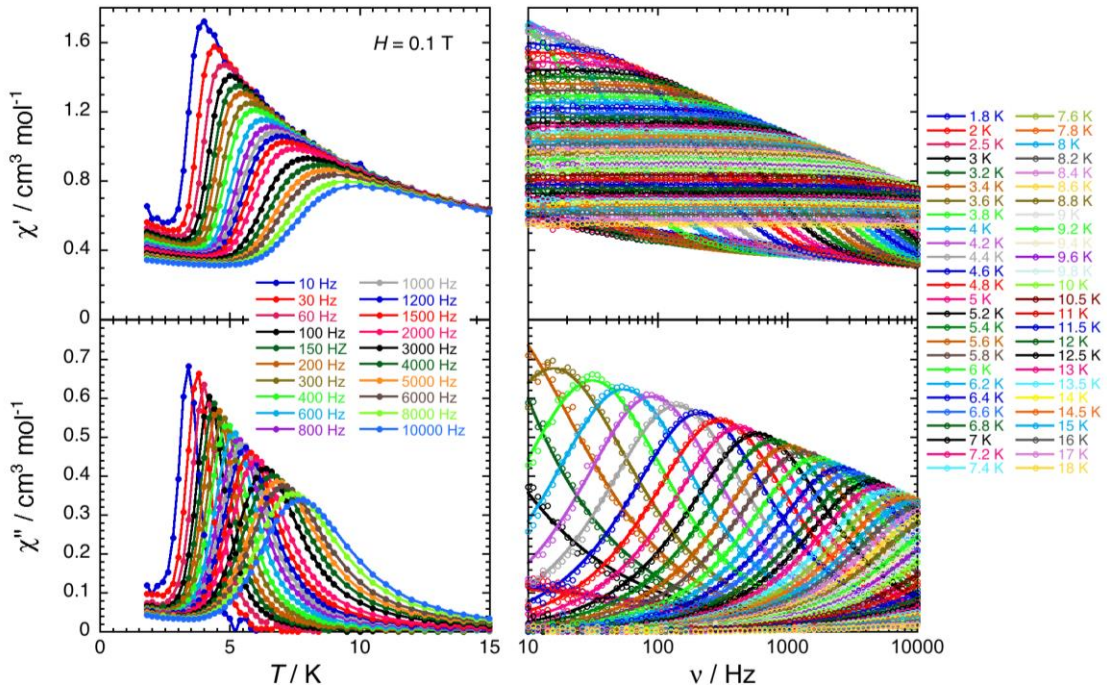


Fig. S28 In-phase (top) and out-of-phase (bottom) components of the molar ac magnetic susceptibility of **3-Dy** measured as a function of temperature at different frequencies (left) and as a function of frequency at different temperatures (right) in 0.1 T dc-field. The solid lines on the left plots are guides for the eyes. The solid lines on the right plots are the generalized Debye fits^{7, 8} of the experimental ac susceptibility data (open dots).

With an eleven-parameter model, it is absolutely unrealistic to fit the experimental data without falling in an overparametrization of the experimental data. Therefore, some experimental observations must be used to simplify the relaxation model and eliminate some contribution(s) in the [equation 1](#). Indeed, the τ versus H , shown on the left part of [Fig. S29](#), is very informative. The relaxation time of **3-Dy** shows a very slow decrease above 0.1 T incompatible with a H^{-4} or H^{-2} variation expected for Direct or Raman ($C_2 < C_1$) processes. As a consequence, and based on [equation 2](#), this field behavior (> 0.1 T) could only be potentially reproduced by an Orbach-like relaxation. At low fields below 0.05 T, the relaxation time is compatible with an H^2 variation expected for QTM or Raman (with $C_2 > C_1$) mechanisms. Therefore, in a first approximation, two simple models involving (i) Raman and Orbach-like, or (ii) QTM and Orbach-like relaxation processes can be considered to fit simultaneously all the experimental data. Indeed, both models are able to reproduce the τ versus H and τ versus T variations in a similar good agreement that is undistinguishable in [Fig. S29](#). Nevertheless, the low value of n (smaller than 1), the lower numbers of adjustable parameters (5 versus 7; with m fixed to 2) and the much larger error bar on the obtained parameters (suggesting overparametrization) favor the second model implying QTM and Orbach-like relaxations. The best set of parameters involving the two last terms of [equation 2](#) are $B_1 = 1.4(1) 10^4 \text{ s}^{-1}$ (or $\tau_{\text{QTM}} = B_1^{-1} \approx 7 10^{-7} \text{ s}$), $B_2 = 5(1) 10^4 \text{ T}^{-2}$, $\tau_0 = 8(2) \times 10^{-8} \text{ s}$, $\Delta/k_B = 43(1) \text{ K}$ ($\Delta_{\text{eff}}/k_B = 37(3) \text{ K}$ in zero-dc field due likely to resonant QTM that shortcuts the total energy barrier),⁹ and $H_0 = 13(2) \text{ T}$. It is important to note that the origin of the Orbach-like relaxation with an energy gap of about 40 K is not obvious for a mononuclear Dy complex, and it should certainly be challenged in future theoretical studies. Even if this model of the relaxation time is able to reproduce well the experimental data with "only" five adjustable parameters ([Fig. S29](#)) and similar approaches have already been used for Dy/COT analogous SMMs,^{10, 11} the physics of the present dynamics might be better described by alternative models, and thus the current analysis should be taken with a great caution as any similar modeling of the relaxation for SMMs.

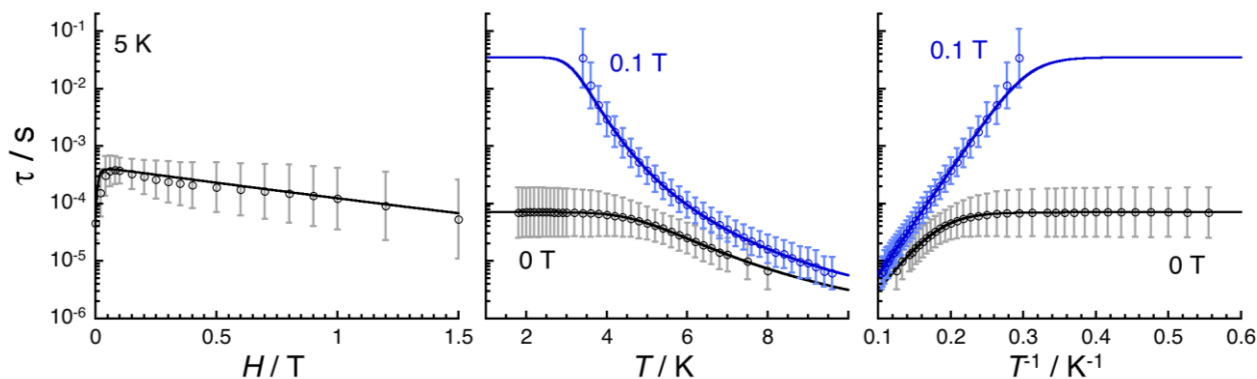


Fig. S29 Relaxation time variation for **3-Dy** as a function of the applied magnetic field at 5 K between 0 and 1.5 T (left) and as a function of the temperature between 1.8 and 10 K plotted as τ vs. T (center) and τ vs. T^{-1} (right) at zero (black open dots) and 0.1 T (blue open dots) dc fields (semi-logarithm plots). The reported relaxation time was estimated from the generalized Debye fits of the ac susceptibility data (Figs. 6, S23, S25, and S26). Estimated standard deviations of the relaxation time (vertical solid bars) have been calculated from the α parameters of the generalized Debye fit (Figs. S23a, S25a, and S26a) and the log-normal distribution as described in reference.⁸ The solid lines are the best fit discussed in the text.

The temperature dependence of the magnetization relaxation time for **5-Er** and its ESD (Fig. S30) were extracted from the experimental ac susceptibility data shown in Fig. 7 and their fit to the generalised Debye model (Fig. S27).^{7, 8} When applying a magnetic field at 27 K, the characteristic frequency of the relaxation mode stays unchanged suggesting that the magnetization relaxation is dominated by an Orbach-like process in this temperature range (Equation 1; among the different processes, Orbach-like relaxation is usually the less field dependent). Nevertheless, the $\ln(\tau)$ versus T^{-1} plot (right part of Fig. S30) is not perfectly linear revealing a departure from a simple thermally activated process. A second relaxation pathway should thus be considered. In zero-dc field, only Raman and QTM are active processes (Equation 2) but only a model considering Raman and Orbach-like relaxations was able to fit all the experimental data (Fig. S30). The best set of parameters are $\tau_0 = 1.3(6) \times 10^{-8}$ s, $\Delta/k_B = 287(16)$ K, $C = 1.4(9) 10^{-12} \text{ s}^{-1} \text{ K}^{-n}$ and $n = 10.4(3)$ (n is in relative good agreement with what is expected for the two-phonon second-order Raman relaxation for a Kramers ion).¹²⁻¹⁴ It is worth mentioning that the characteristics of the Orbach-like process are indeed very similar to those estimated in related Er/COT complexes.^{10, 15, 16}

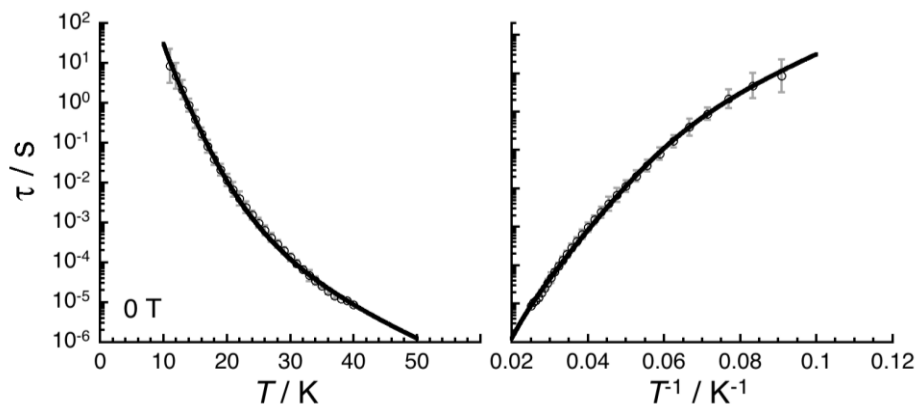


Fig. S30 Relaxation time variation for **5-Er** as a function of the temperature between 1.85 and 60 K plotted as τ vs. T (left) and τ vs. T^{-1} (right) at zero dc field (semi-logarithm plots). The reported relaxation time was estimated from the generalized Debye fits of the ac susceptibility data shown in Fig. 7. Estimated standard deviations of the relaxation time (vertical solid bars) have been calculated from the α parameters of the generalized Debye fit (Fig. S27) and the log-normal distribution as described in reference.⁸ The solid line is the best fit discussed in the text.

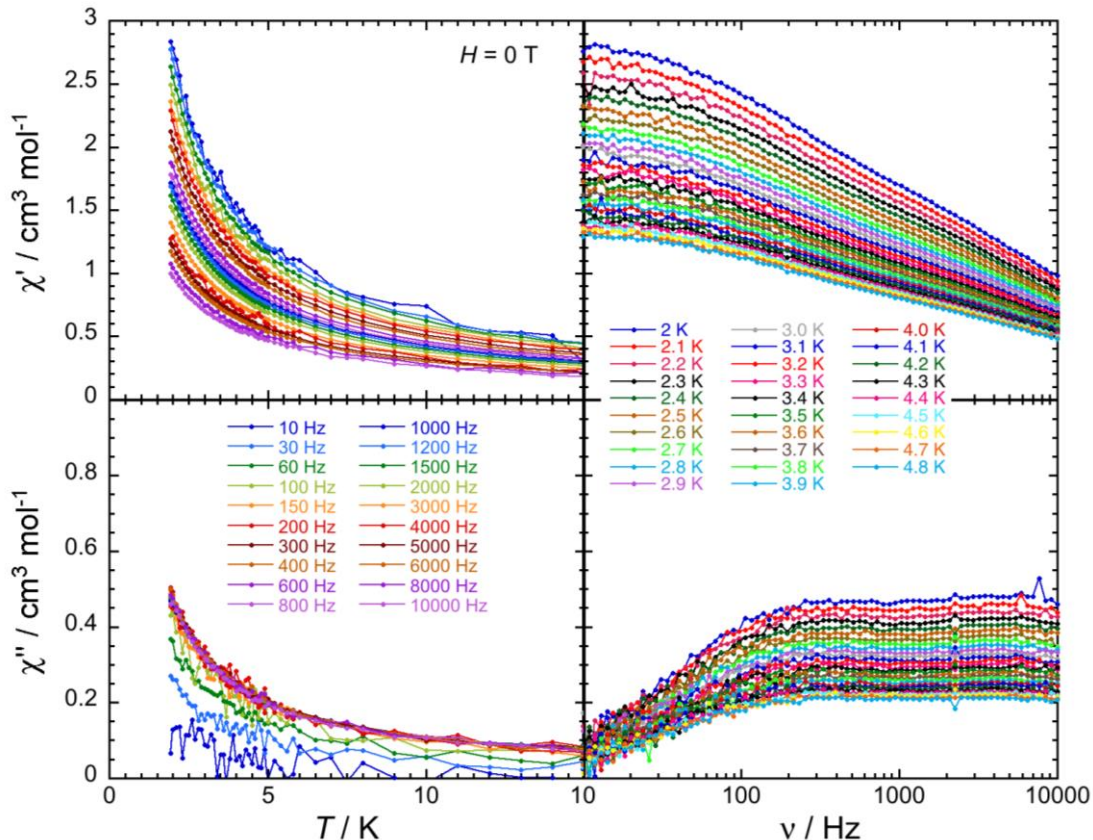


Fig. S31 In-phase (top) and out-of-phase (bottom) components of the molar ac magnetic susceptibility of **6-Tm** measured as a function of temperature at different frequencies (left) and as a function of frequency at different temperatures (right) in zero dc-field.

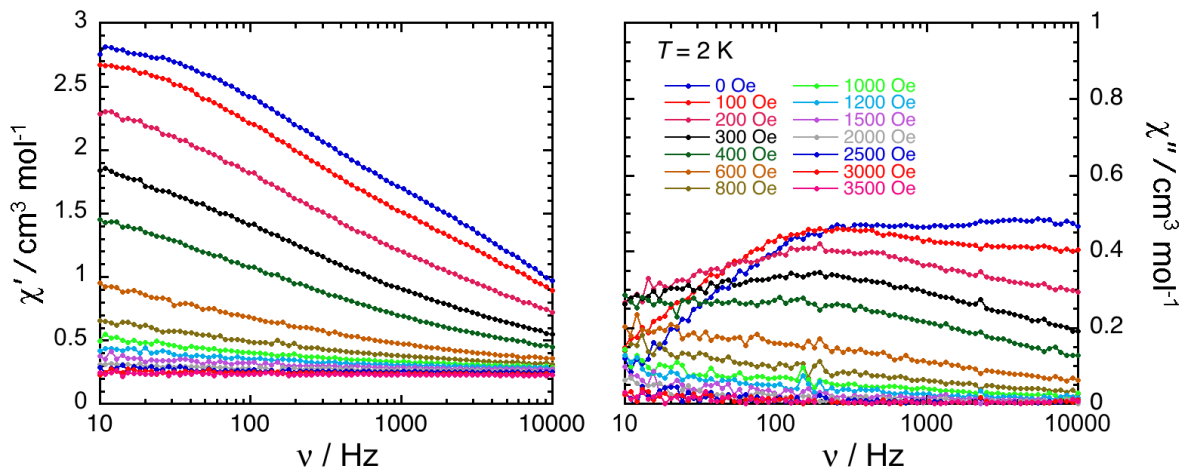


Fig. S32 ac frequency dependences (between 10 and 10000 Hz) of the real (χ' , top) and imaginary (χ'' , bottom) parts of the ac susceptibility for **6-Tm** at 2 K and under an applied dc field varying between 0 and 0.35 T.

VI. Computational Methods

The positions of hydrogen atoms in **1–7** were optimized with Grimme's composite PBEh-3C¹⁷ method using the ORCA electronic structure package, version 5.¹⁸⁻²⁰ The equilibrium structures were then subjected to single point evaluations at the PBE0²¹ and strongly-contracted NEVPT2($n,7$)²²⁻²⁴ levels using the RIJCOSX²⁵⁻²⁹ approximation, where n is the relevant number of f-electrons in the complex. Scalar relativistic corrections were accounted for with the Zeroth-Order Regular Approximation (ZORA). The lanthanide centers were modeled with the SARC2-ZORA-QZVP³⁰⁻³³ basis set, and all other atoms were treated with the ZORA-def2-TZVP basis set. Natural bond orbital analysis was performed on top of the converged PBE0 wavefunctions using NBO 7.0.³⁴

Magnetic properties were evaluated using state-averaged CASSCF($n,7$) and NEVPT2($n,7$) wavefunctions, where state-averaged orbitals were used for each state in the NEVPT2 treatments (the so-called canonstep 0 in ORCA terminology). Full intermediate coupling was used for each complex. Spin-orbit coupling was included with quasi-degenerate perturbation theory (QDPT) using the SA-CASSCF wavefunction and strongly contracted NEVPT2 diagonal energies.³⁵ Ground state multiplet analysis was performed for CASSCF results with help of SINGLE_ANISO³⁶⁻³⁸ approach as implemented in ORCA. Relativistic effects were included by using the spin-orbit mean field operator.

Table S13 Energy spectrum of $|M_J|$ states for ground state multiplets of **2–7** calculated at the CASSCF($n,7$) level. Columns in red are non-Kramers ions and the $|M_J|$ labels are on the right, while blue columns are Kramers ions with $|M_J|$ labels on the left

$ M_J $	2-Tb	3-Dy	4-Ho	5-Er	6-Tm	7-Yb	$ M_J $
	7F_6	$^6H_{15/2}$	5I_8	$^4I_{15/2}$	3H_6	$^2F_{7/2}$	
15/2		986.5	515.2	0.0			8
13/2		244.3	351.9	189.2			7
11/2	636.2	28.5	137.1	409.9	0.0		6
9/2	696.6	0.0	0.0	526.7	696.8		5
7/2	848.6	45.5	10.9	513.4	872.4	174.9	4
5/2	407.5	98.2	78.6	412.1	860.5	0.0	3
3/2	180.6	154.7	193.0	291.7	822.2	553.3	2
1/2	45.0	134.4	291.1	214.2	780.7	907.5	1
	0.0		329.3		761.5		0

Table S14 Magnetic properties of the two lowest energy $|M_J|$ states in the ground state multiplet for **2–7** at the CASSCF($n,7$) level. θ is the angle between the g_z axes, and ζ is the SOC constant calculated at the NEVPT2($n,7$) level of theory

	2-Tb	3-Dy	4-Ho	5-Er	6-Tm	7-Yb
$ M_J $	0	9/2	9/2	15/2	6	5/2
g_x	0	0.0206	$3.1e^{-7}$	$6.9e^{-7}$	0.0	0.0117
g_y	0	0.0890	$4.1e^{-7}$	$8.1e^{-7}$	$6.0e^{-8}$	0.0350
g_z	0	12.5883	10.9591	17.9424	13.9776	5.7310
$ M_J $	1	11/2	7/2	13/2	5	7/2
g_x	0	0.0104	$3.7e^{-7}$	0.0019	0.0	0.0113
g_y	$8.0e^{-8}$	0.0328	$4.2e^{-7}$	0.0019	$5.0e^{-8}$	0.0115
g_z	3.3132	14.3627	12.7992	15.5256	11.5846	7.9985
θ ($^\circ$)	N/A	22.6	38.8	0.17	1.3	5.4
ζ (cm^{-1})	1698.81	1894.24	2105.13	2332.05	2576.56	2831.59

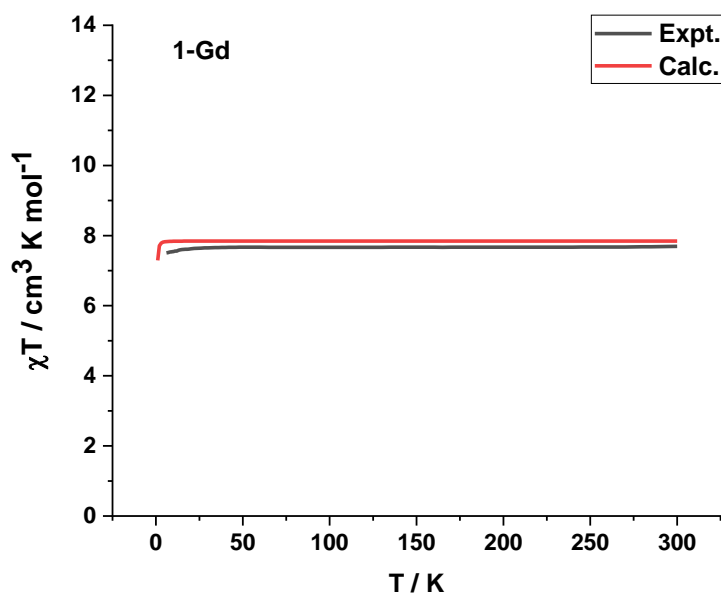


Fig. S33 Calculated (red) and experimental χT curves for **1-Gd**.

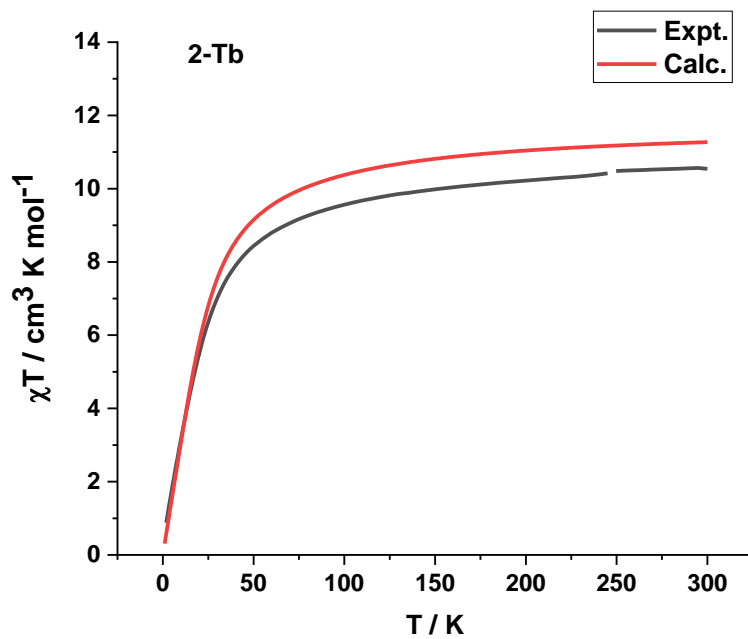


Fig. S34 Calculated (red) and experimental χT curves for **2-Tb**.

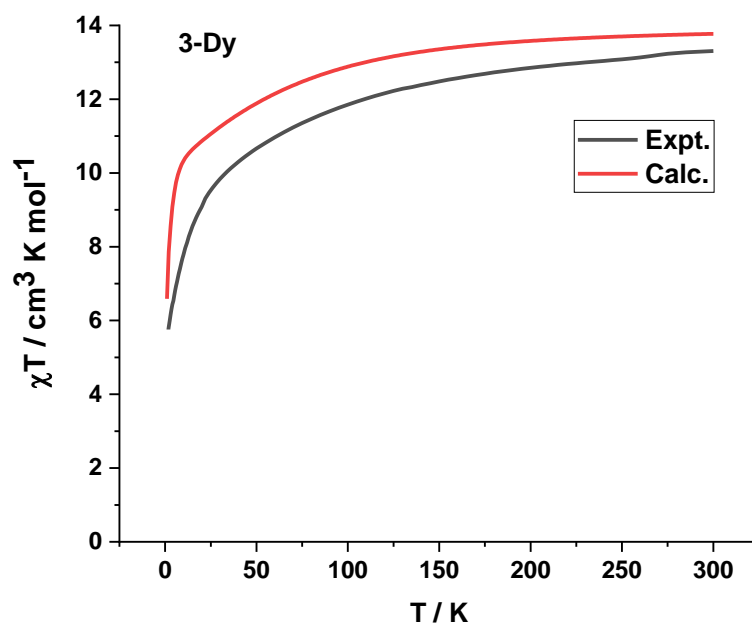


Fig. S35 Calculated (red) and experimental χT curves for **3-Dy**.

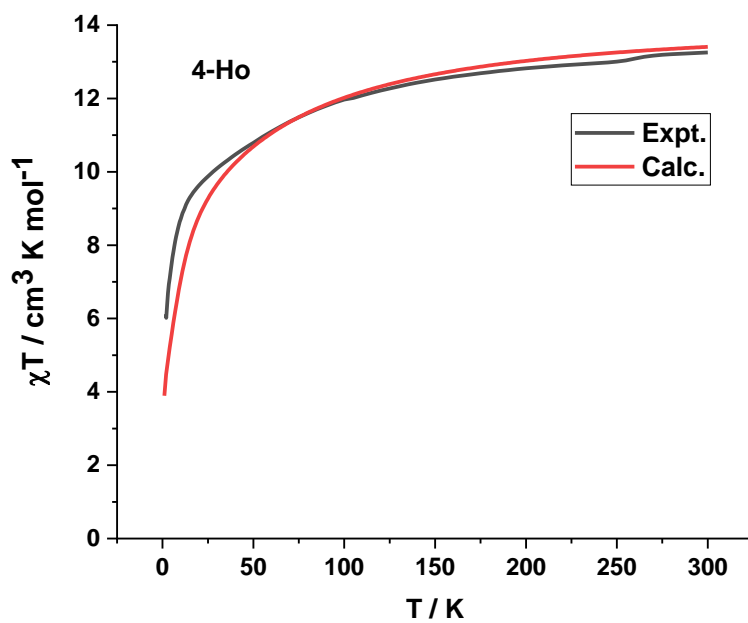


Fig. S36 Calculated (red) and experimental χT curves for **4-Ho**.

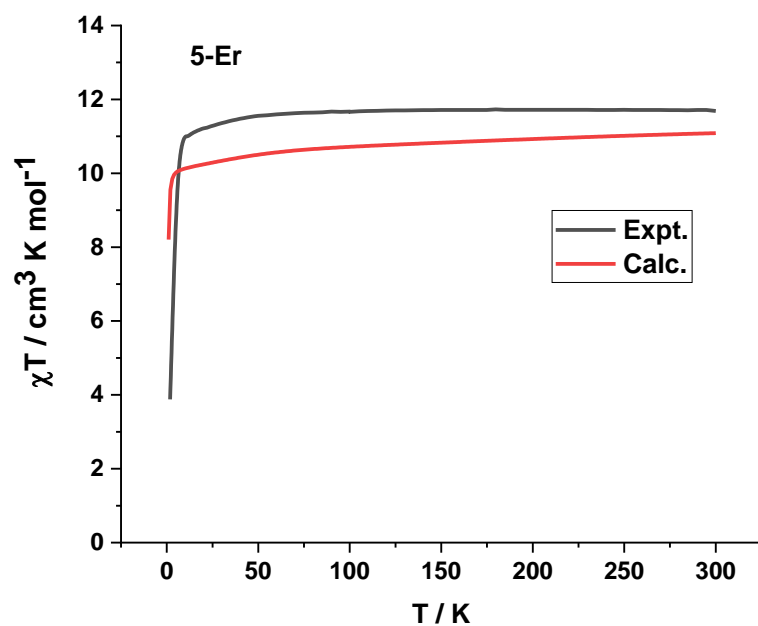


Fig. S37 Calculated (red) and experimental χT curves for **5-Er**.

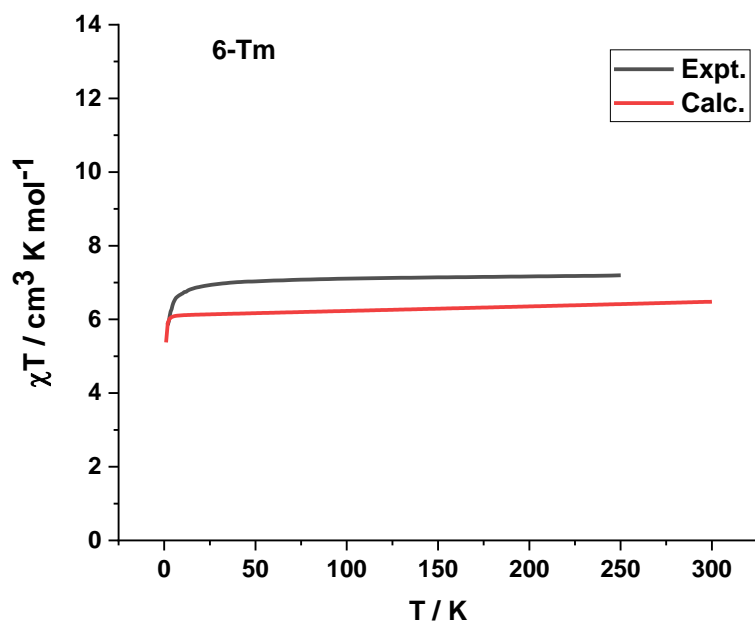


Fig. S38 Calculated (red) and experimental χT curves for **6-Tm**.

VII. References

1. N. V. Kozhemyakina, J. Nuss and M. Jansen, *Z. Anorg. Allg. Chem.*, 2009, **635**, 1355-1361.
2. Z. Zhou, J. Greenough, Z. Wei and M. A. Petrukhina, *Acta Crystallogr., Sect. C: Struct. Chem.*, 2017, **73**, 420-423.
3. SAINT; part of Bruker APEX3 software package (version 2017.3-0): Bruker AXS, 2017.
4. SADABS; part of Bruker APEX3 software package (version 2017.3-0): Bruker AXS, 2017.
5. G. M. Sheldrick, *Acta Crystallogr.*, 2015, **A71**, 3-8.
6. G. M. Sheldrick, *Acta Crystallogr.*, 2015, **C71**, 3-8.
7. K. S. Cole and R. H. Cole, *J. Chem. Phys.*, 1941, **9**, 341-351.
8. D. Reta and N. F. Chilton, *PCCP*, 2019, **21**, 23567-23575.
9. D. Gatteschi, R. Sessoli and J. Villain, *Molecular Nanomagnets*, Oxford University Press, Oxford, 2006.
10. L. Ungur, J. J. Le Roy, I. Korobkov, M. Murugesu and L. F. Chibotaru, *Angew. Chem. Int. Ed.*, 2014, **53**, 4413-4417.
11. J. J. Le Roy, M. Jeletic, S. I. Gorelsky, I. Korobkov, L. Ungur, L. F. Chibotaru and M. Murugesu, *J. Am. Chem. Soc.*, 2013, **135**, 3502-3510.
12. K. N. Shrivastava, *Phys. Stat. Sol. B*, 1983, **117**, 437-458.
13. J. H. Van Vleck, *Phys. Rev.*, 1940, **57**, 426-447.
14. A. Abragam and B. Bleaney, *Electron Paramagnetic Resonance of Transition Ions*, Dover, New York, 1986.
15. J. J. Le Roy, L. Ungur, I. Korobkov, L. F. Chibotaru and M. Murugesu, *J. Am. Chem. Soc.*, 2014, **136**, 8003-8010.
16. K. R. Meihaus and J. R. Long, *J. Am. Chem. Soc.*, 2013, **135**, 17952-17957.
17. S. Grimme, J. G. Brandenburg, C. Bannwarth and A. Hansen, *J. Chem. Phys.*, 2015, **143**, 054107.
18. F. Neese, *Wiley Interdiscip. Rev.: Comput. Mol. Sci.*, 2012, **2**, 73-78.
19. F. Neese, *ORCA – An Ab Initio, DFT and Semiempirical SCF-MO Package, Ver. 4.0*, Max Planck Institute for Chemical Energy Conversion, Mülheim a. d. Ruhr, Germany, 2017.
20. F. Neese, *Wiley Interdiscip. Rev.: Comput. Mol. Sci.*, 2018, **8**, e1327.
21. A. D. Becke, *J. Chem. Phys.*, 1993, **98**, 1372-1377.
22. C. Angeli, R. Cimiraglia and J.-P. Malrieu, *Chem. Phys. Lett.*, 2001, **350**, 297-305.
23. C. Angeli, R. Cimiraglia, S. Evangelisti, T. Leininger and J. P. Malrieu, *J. Chem. Phys.*, 2001, **114**, 10252-10264.
24. C. Angeli, B. Bories, A. Cavallini and R. Cimiraglia, *J. Chem. Phys.*, 2006, **124**, 054108.
25. F. Neese, *J. Comput. Chem.*, 2003, **24**, 1740-1747.
26. F. Neese, F. Wennmohs, A. Hansen and U. Becker, *Chem. Phys.*, 2009, **356**, 98-109.
27. S. Kossmann and F. Neese, *Chem. Phys. Lett.*, 2009, **481**, 240-243.
28. R. Izsák and F. Neese, *J. Chem. Phys.*, 2011, **135**, 144105.
29. D. Ganyushin, N. Gilka, P. R. Taylor, C. M. Marian and F. Neese, *J. Chem. Phys.*, 2010, **132**, 144111.
30. D. Aravena, F. Neese and D. A. Pantazis, *J. Chem. Theory Comput.*, 2016, **12**, 1148-1156.

31. J. Chmela and M. E. Harding, *Mol. Phys.*, 2018, **116**, 1523-1538.
32. F. Weigend, *PCCP*, 2006, **8**, 1057-1065.
33. F. Weigend and R. Ahlrichs, *PCCP*, 2005, **7**, 3297-3305.
34. E. D. Glendening, J. K. Badenhop, A. E. Reed, J. E. Carpenter, J. A. Bohmann, C. M. Morales, P. Karafiloglou, C. R. Landis and F. Weinhold, *NBO 7.0*, University of Wisconsin, Madison, WI, 2018.
35. D. Ganyushin and F. Neese, *J. Chem. Phys.*, 2006, **125**, 024103.
36. L. F. Chibotaru and L. Ungur, *J. Chem. Phys.*, 2012, **137**, 064112.
37. N. Iwahara, L. Ungur and L. F. Chibotaru, *Phys. Rev. B*, 2018, **98**, 054436.
38. L. Ungur and L. F. Chibotaru, *Chem. - Eur. J.*, 2017, **23**, 3708-3718.